Bachelor thesis

Study of a novel compact beam line at a medical cyclotron

Author:
Diana Wüthrich

Supervisor:
PD Dr. Saverio Braccini

26th August 2016

University of Bern

Albert Einstein Center for fundamental physics

Laboratory for High Energy Physics

Contents

Introduction

To study and produce novel radioisotopes for medicine, beams of specific shape and intensity are necessary. For this purpose, a compact beam transport line was developed and is under test at the Bern medical cyclotron laboratory which provides proton beams for the production of radioisotopes for Positron Emission Tomography (PET) and for research activities. Unlike in Bern, medical cyclotrons are usually not equipped with an about 6 m long Beam Transport Line and an about 1 m long compact Mini Beam Line would be very useful in order to manipulate shape and position of the beam. The goal is to irradiate the target flat and precisely at the right position, since the target material can be very expensive and therefore very small.

In this thesis, the candidate performed experimental measurements and simulations of the proton beam shaped by the first prototype of the Mini Beam Line by means of specific particle detectors called UniBEaM. The objective was to obtain first results, which means to test whether the focusing and defocusing as well as the steering properties of the novel compact beam line work qualitatively well. A few quantitative results could also be obtained.

In the first chapter of this thesis, the basic principles of cyclotrons and their use for PET-radioisotope production will be explained, an overview of the Bern cyclotron laboratory will be given and beam transport physics will be introduced. All used devices as well as the experimental set-up are described and discussed in the second chapter. The simulation of the Mini Beam Line is described in chapter 3, followed by the experimental measurements, results and conclusions in chapter 4.

1 Cyclotrons and beam transport

A cyclotron is a particle accelerator which was first conceived and constructed by Ernest Orlando Lawrence and Milton Stanley Livingston in 1931 [1, 2]. Today, its main application field lies in medicine. On one hand, there is the radioisotope production for PET (Positron Emission Tomography) imaging, which is done at the Bern medical cyclotron and is described below, and on the other hand there is proton therapy against cancer. In connection with particle accelerators, beam transport plays an important role which is also explained in this chapter.

1.1 Positron Emission Tomography

Positron Emission Tomography (PET) is one of the most important functional imaging techniques, which means that a three dimensional image of the human body is made on the basis of a biological function as for example the sugar consumption of cells. This is one of the methods to detect and localize cancer [3].
The ion beam from the cyclotron hits a target in which a nuclear reaction is produced. The target becomes radioactive. In Bern, the fluorine isotope ^{18}F with a half-life of 110 minutes is produced daily. After its production, it is chemically synthesized in 18-fluoro-deoxy-glucose (FDG) which is an analog to glucose. This radiotracer is injected in the patient. It spreads out in the body through blood circulation. Afterwards, it is transported into the cells in the same way as glucose. Since tumor cells consume a lot of energy, the concentration of the radioactive FDG will be high there compared to the healthy cells. Through a β^+ decay, a positron is emitted and travels a short distance before annihilating with an electron. The two characteristic back-to-back 511 keV photons are simultaneously detected by a PET scanner. From this information, a three dimensional image can be reconstructed [3].

1.2 Cyclotron physics

The working principle of a cyclotron is very simple (figure 1). In the middle of the cylindrical space, the ion source is located, from where H^- ions are emitted. In the accelerating gap, they gain velocity through a fast varying electric field which operates at radio frequency (RF). A static magnetic field holds the particles on a spiral trajectory.

The frequency of the alternating electric field has to be correctly chosen in order to get an acceleration. The Lorentz force $\vec{F}_L$ acts on the particle and using Newton's law, we get

$$\vec{F}_L = m\vec{a} \tag{1.1}$$

$$\Longrightarrow \qquad q\left|\vec{v} \times \vec{B}\right| = \frac{mv^2}{r}, \tag{1.2}$$

where q is the electric charge and m the mass of the particle. Since the velocity of the particle $\vec{v}$ is orthogonal to the magnetic field $\vec{B}$ (figure 1), this reduces to

$$qvB = \frac{mv^2}{r} \qquad \Longrightarrow \qquad v = \frac{qBr}{m}. \tag{1.3}$$

The rotation frequency is therefore given by

$$\nu_c = \frac{v}{2\pi r} = \frac{qB}{2\pi m}. \tag{1.4}$$

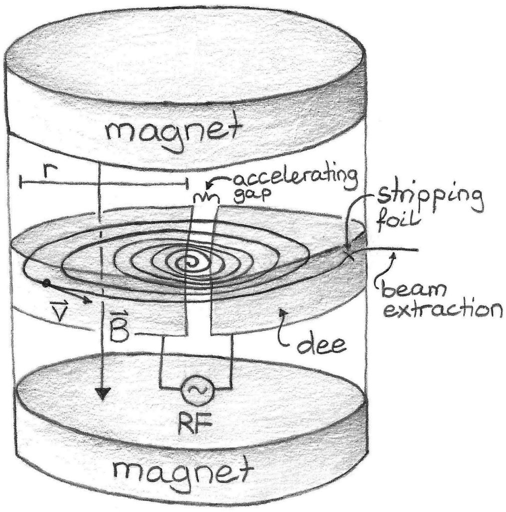

Figure 1: Working principle of a cyclotron.
The two magnets generate a homogeneous, static magnetic field keeping the particle with velocity $\vec{v}$ and distance to the centre r on its spiralling trajectory. Between the two dees, the RF alternating voltage accelerates the particles in the accelerating gap. The beam extraction is performed with a stripping foil.

This frequency is independent of the radius and is called the cyclotron frequency. It only depends on the B-field and the q/m ratio of the particle. At the Bern medical cyclotron with an average magnetic field of 1.4 T, it is 21 MHz for H^- ions. All even harmonics then lead to acceleration, since the geometry of the two dees (figure 2) is more complicated as it is drawn in figure 1 [3].

In Bern, the extraction is performed by stripping, which means that two electrons are taken away from the H^- ions by stripping foils. The remaining protons have opposite charge and are therefore bended the other way round by the magnetic field. They leave the cyclotron through one of the eight extraction ports [3].

1.3 The Bern cyclotron laboratory

The Bern medical cyclotron, which is the core element of the laboratory, was constructed by the company Ion Beam Applications (IBA) in Belgium (figure 2). It has a maximal beam energy of about 18 MeV and accelerates H^- (and D^- as an option). It is 2 m in diameter and 2.2 m high. The cyclotron is situated in a bunker with a 6.5 m long Beam Transport Line (BTL) going to another bunker (figure 3). This is because the radio isotope production and the research activities should not interfere. The wall between the bunkers is 1.8 m thick due to radiation protection [3].

The Bern cyclotron laboratory is situated in the campus of the Inselspital. The SWAN (which stands for SWiss hAdroNs) project was founded by the University Hospital in Bern (Inselspital) and the University of Bern in order to produce radio tracers for the PET imaging at Inselspital as well as for other healthcare institutions and to perform multidisciplinary research activities. The initial steps of the collaboration were taken in 2007. In 2010, the construction phase started and in February 2012, the first ion beams were accelerated. The laboratory gained the fully operational status in the end of 2012 [3].

Figure 2: The Bern medical cyclotron opened during commissioning. Extraction port four is connected to the BTL whose first quadrupole doublet is located in the cyclotron bunker [3].

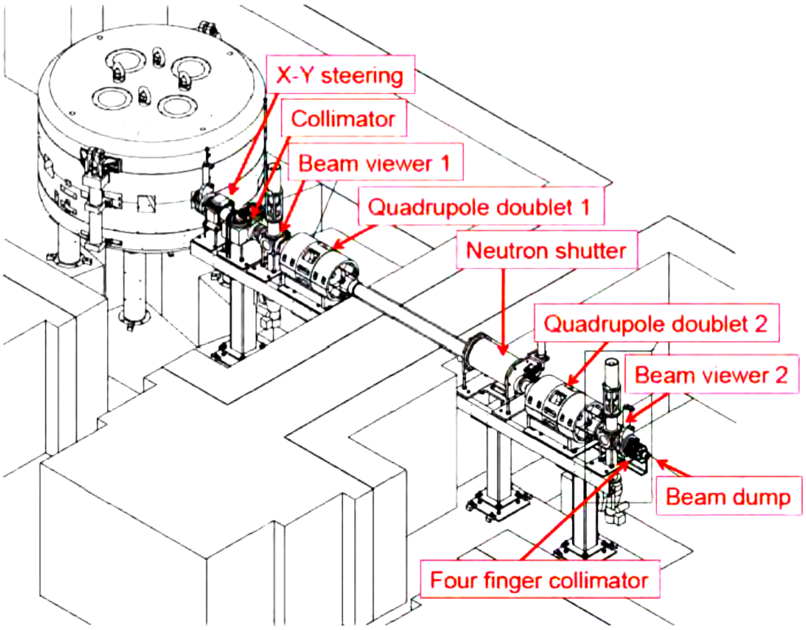

Figure 3: Schematic view of the BTL connecting the two bunkers at the Bern cyclotron laboratory, in which all essential elements are indicated [3].

1.4 Beam transport

The Lorentz force generated by the electromagnetic field determines the trajectory of charged particles

$$\vec{F}_L = q(\vec{E} + \vec{v} \times \vec{B}). \tag{1.5}$$

Subsequent explanations follow [4], [5] and [6]. In a beam transport line, focalisation and bending of the beam is performed using magnets. For this reason, the electrical field $\vec{E}$ is set to zero and we assume static magnetic fields. The multipole expansion of the magnetic field gives us the dipole, quadrupole and higher order terms. In this Bachelor thesis, higher order terms are neglected. For an ideal beam, the dipole terms bend the particles and the quadrupole terms correct for small displacements from the ideal path, ensuring stability of the beam.
A dipole magnet produces an uniform magnetic field. It holds a particle with a certain velocity and electric charge on a circular orbit as calculated in section 1.2.

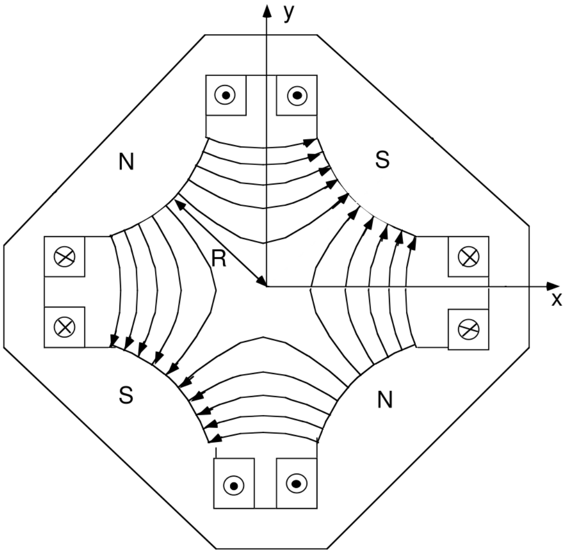

Figure 4: Transverse section of a quadrupole magnet with bore radius R using four electric coils. The magnetic field lines are indicated.

The most common realization of a quadrupole magnetic field is performed with four coils as shown in figure 4. At the centre of the magnet, the magnetic field is equal to zero. Therefore, only particles outside the ideal trajectory are affected by the field which results in focusing or defocusing. For an ideal beam propagating along the symmetry axis of the quadrupole magnet, it does not affect the beam direction. The quadrupole strength k determines how much the beam will be focused or defocused passing through the quadrupole magnet. It depends on the magnetic field gradient B' in the plane orthogonal to the beam as well as the momentum over charge ratio p/q. It is defined as

$$k^2 = \frac{B'}{p/q}. \tag{1.6}$$

The electromagnetic field generated by a quadrupole magnet does not end sharply at the edges (figure 5). It well extends the length of the iron core and, therefore, the effective magnetic length L is longer than the iron length $\tilde{L}$ by about one half of the bore diameter d_b

$$L \approx \tilde{L} + \frac{1}{2} d_b. \tag{1.7}$$

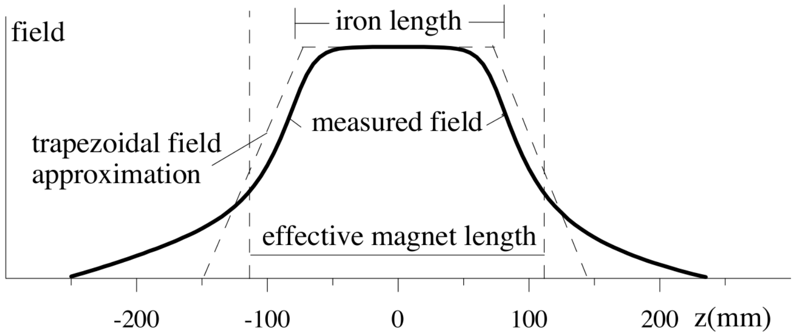

Figure 5: Field profile in the beam direction in a real quadrupole magnet with a bore diameter d_b of 6 cm and an iron length $\tilde{L}$ of 15.9 cm. The iron and the effective length are indicated as well as the trapezoidal field approximation which will not be used in this thesis (p. 125 in [4]).

In order to treat the beam transport mathematically, an orthogonal right-handed coordinate system which moves with an ideal particle along the central trajectory of the transport system is defined. The unit vector z is the coordinate tangential to the central trajectory and points in the direction of motion. The transverse coordinates x and y measure the displacement of a particle from the central trajectory. Thus, the phase space is defined as follows:

$$\begin{pmatrix} x \\ x' \\ y \\ y' \\ l \\ \delta \end{pmatrix} := \begin{pmatrix} \text{horizontal displacement of trajectory with respect to central trajectory} \\ \text{angle the particle makes in horizontal plane with respect to central trajectory} \\ \text{vertical displacement of trajectory with respect to central trajectory} \\ \text{angle the particle makes in vertical plane with respect to central trajectory} \\ \text{path length difference between particle and central trajectory} \\ \text{fractional momentum deviation of particle from central trajectory } (\Delta p/p_{tot}) \end{pmatrix}.$$

For our study, the path length difference l is not a relevant quantity. Therefore, the phase space will be limited to the five dimensions (x, x', y, y', δ).

The trajectory equation in paraxial approximation can be obtained using Newton's law. Assuming no magnetic field in the direction along the ideal path and considering only linear terms in x, x', y, y' and δ, we get the general trajectory equation which can be written in a matrix formalism. The so-called transfer matrix is multiplied to the phase space vector, which results in a new phase space vector describing the beam after having passed the magnetic field. For idealized fields consisting of separated beam line elements, the resulting transfer matrix is the product of all transfer matrices of the several elements. In this thesis, the drift space and quadrupole magnet will be used.

The propagation of the beam through a drift length L is then given by

$$\begin{pmatrix} x_2 \\ x'_2 \\ y_2 \\ y'_2 \\ \delta_2 \end{pmatrix} = \begin{pmatrix} 1 & L & 0 & 0 & 0 \\ 0 & 1 & 0 & 0 & 0 \\ 0 & 0 & 1 & L & 0 \\ 0 & 0 & 0 & 1 & 0 \\ 0 & 0 & 0 & 0 & 1 \end{pmatrix} \begin{pmatrix} x_1 \\ x'_1 \\ y_1 \\ y'_1 \\ \delta_1 \end{pmatrix}.$$

For a quadrupole magnet, the transfer matrix is

$$\begin{pmatrix} \cosh(kL) & \frac{1}{k}\sinh(kL) & 0 & 0 & 0 \\ k\sinh(kL) & \cosh(kL) & 0 & 0 & 0 \\ 0 & 0 & \cos(kL) & \frac{1}{k}\sin(kL) & 0 \\ 0 & 0 & -k\sin(kL) & \cos(kL) & 0 \\ 0 & 0 & 0 & 0 & 1 \end{pmatrix},$$

where k is the quadrupole field strength (equation 1.6) and L the effective length of the quadrupole (equation 1.7). The two matrices are block diagonal which means that the x, y and z motions are decoupled under the approximations mentioned above. In addition, the δ matrix entries are equal to 1 which causes an identity transformation in the corresponding entries of the phase space vectors. Therefore, the δ-component will not be mentioned any more from now on.

Apart from the energy, mass and charge of the particles as well as the number of particles, the beam properties are usually expressed with the beam matrix σ which should not be confused with the beam transfer matrix introduced above. The x-component of this σ-matrix writes in the following way

$$\sigma_x = \begin{pmatrix} \sigma_{11} & \sigma_{12} \\ \sigma_{21} & \sigma_{22} \end{pmatrix} = \begin{pmatrix} \langle x^2 \rangle & \langle xx' \rangle \\ \langle xx' \rangle & \langle x'^2 \rangle \end{pmatrix},$$

where $\langle x^2 \rangle$ and $\langle x'^2 \rangle$ are the expectation values of x^2 and x'^2 respectively and $\langle xx' \rangle$ is the covariance. The x-component of the transverse beam emittance ϵ is then given by the square root of the determinant of σ_x

$$\epsilon_x = \sqrt{\det(\sigma_x)}. \tag{1.8}$$

The y-component of the beam matrix and the corresponding transverse beam emittance is analog to the x-component. Taking now the total beam transfer matrix R of any number of beam line elements, one can find the new beam matrix after the beam having passed these beam line elements in the following way

$$\sigma' = R\sigma R^T. \tag{1.9}$$

1.5 Vacuum

Beam transport can only take place in vacuum, since the particles would loose too much energy going through air and be stopped. In this Bachelor thesis, two pump types were used. Rotary pumps use a system to repetitively expand a cavity, allow gases to flow in from the chamber, seal off the cavity and let it out to the atmosphere. Momentum transfer pumps use high speed rotating blades or high speed jets of dense fluid to transport gas molecules out of the chamber. It is usually a turbo molecular pump or an oil diffusion pump which both fulfil the same purpose. The oil diffusion pump, however, is more suitable for continuous use.

Rotary pumps are very effective to establish a pre-vacuum starting from atmospheric pressure. Momentum transfer pumps, in contrast, can only start pumping when there are just single molecules flying around in the chamber. Through continuous desorption of the chamber wall and of polar materials like water, fat or dust sticking at the surfaces, the pressure reaches an equilibrium at about 10^{-7} Torr. It is obvious to connect the rotary and the momentum transfer pump in series (figure 6). In order to reach even deeper pressures than 10^{-7} Torr, one would need another technology. In the Bern medical cyclotron and its Beam Transport Line, the vacuum pressure is about 10^{-6} Torr and these two pump systems are enough.

Following the standard procedure, we first turn on the rotary pump which we also call primary pump. At a pressure of about $5 \cdot 10^{-2}$ Torr, we turn on the momentum transfer pump which is named secondary pump. Plotting the pressure as a function of the time, we expect a logarithmic decay and a clear step at the time we turn on the secondary pump (figures 15 and 16 in chapter 4).

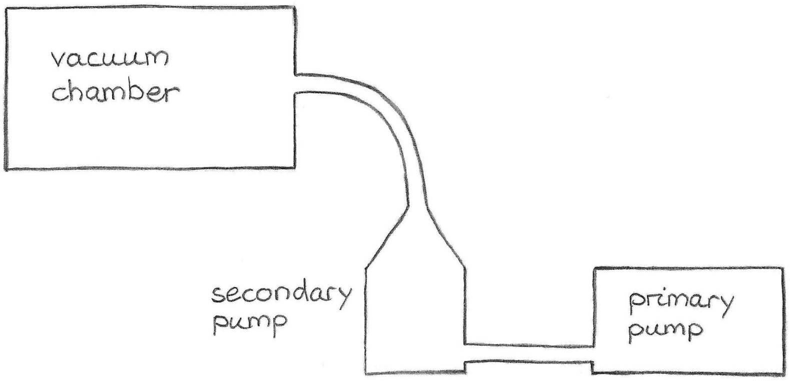

Figure 6: Working principle of the described pumping system.
The vacuum chamber is connected to the secondary pump (turbo molecular or oil diffusion pump) and this one to the primary pump (rotary pump).

2 The Mini Beam Line and the UniBEaM detector

In this chapter, the measurement devices used in this Bachelor thesis as well as the experimental set-up and procedures of the different experiments (section 2.3) will be explained.
The Mini Beam Line is a compact, light-weight beam line designed in order to optimize the beam on the target for the use in PET radioisotope production with the gain of improving production rates (section 2.1) [7, 8]. In order to measure the novel beam line's focusing and steering properties, two UniBEaM detectors are used (section 2.2).

2.1 The Mini Beam Line

The following information is taken from the documentation by the Canadian company, Dehnel – Particle Accelerator Components and Engineering Inc. (D-PACE), manufacturer of the novel compact beam line [7, 8].

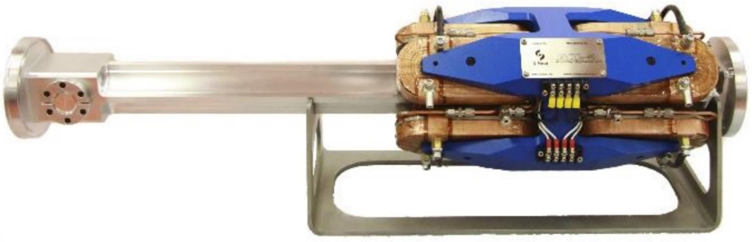

Figure 7: The Mini Beam Line [8].

The Mini Beam Line (figure 7) consists of a short, unique aluminium beam pipe, allowing high transmission and low activation, and a compound quadrupole doublet steering magnet made out of eight coils. This magnet has both horizontal and vertical focusing, as well as horizontal and vertical steering functions and can freely be positioned along the beam tube. The beam tube lengths and flange sizes can also be easily custom tailored to precisely fit existing equipment, making upgrades less complicated. The Mini Beam Line is connected to four power supplies and to a water cooling system. It is made out of radiation resistant materials reducing activation, needs practically no maintenance and is ideal for the use with 12-19 MeV proton beams. In addition, it shifts the target away from the cyclotron, allowing the possible use of local shielding to reduce residual activation. Its general specifications are listed in table 1.

Mass	54 kg
Length	906 mm
Quadruple slope	33 G/A
Maximum steering angle	6.5 mrad for 12.6 MeV protons when operating without quadrupoles

Table 1: General specifications of the Mini Beam Line.

The properties of both quadrupole and steering magnets are listed in table 2. The steering magnets bend linearly with their operating currents. However, as all four component magnets (two quadrupole and two steering magnets) share a single yoke and are embedded in a single magnet, variation of the current in one coil will affect the others. This non-linear effects have to be taken into consideration when tuning the Mini Beam Line.

	Quadrupole magnets	**Steering magnets**
Front coils	Horizontal focusing	Vertical steering
Back coils	Vertical focusing	Horizontal steering
Maximum magnetic field	2500 G	230 G
Operating current	0 A to 75 A	0 A to 10 A
Power supply voltage	0 V to 8 V	0 V to 10 V

Table 2: General specifications of the quadrupole and steering magnets.

2.2 The UniBEaM detector

The Universal Beam Monitor (UniBEaM) is a non-interceptive transverse beam profiler operating in a wide current range from 1 pA to tens of μA and is based on doped silica and optical fibers. It has been conceived and designed at the Laboratory for High Energy Physics (LHEP) which is part of the Albert Einstein Center for fundamental physics (AEC) in Bern. It is simple, compact, robust, easy to operate and can measure pulsed as well as continuous beams. The industrialization of the detector is performed in collaboration with the company D-PACE [9, 7].

The working principle of this beam monitor is simple. A doped silica scintillation fiber moves transversally across the beam. Charged particles passing through the fiber cause scintillation and yielded light is transported via an optical fiber, which is coupled to the scintillation fiber, to a photomultiplier tube (PMT) or to a photodiode. This signal is digitized by an analog to digital converter (ADC). From there, the number of counts is transferred to the computer. A motor sends the position information of the doped silica fiber via an RS-232 cable to the computer where the beam profile, number of counts as a function of the position, is plotted online and stored. The motor moves the fiber stepwise through the beam with an arbitrary step size. Between these movement steps, light intensity measurements are performed in the time when the fiber stands still [9].
The UniBEaM detector is installed in the beam line bunker of the Bern cyclotron laboratory while all electronic devices are located in the physics laboratory and therefore protected from radiation by means of the bunker wall and always accessible to use (figure 8).

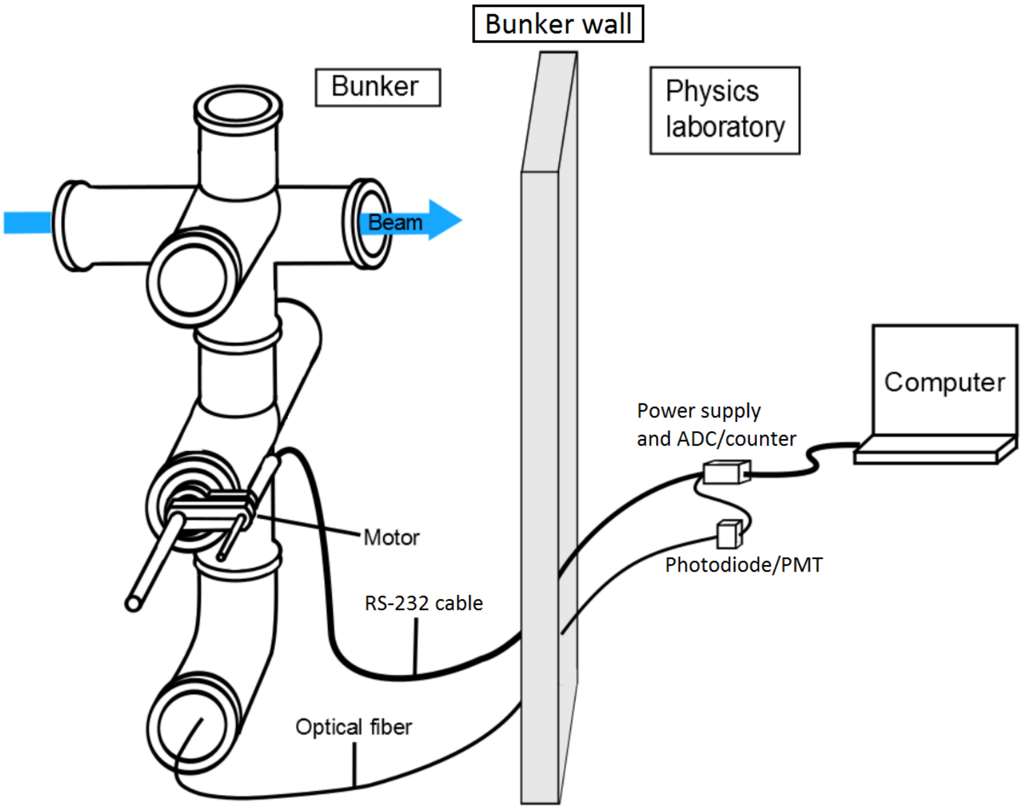

Figure 8: Experimental set-up of the UniBEaM detector installed in the beam line bunker in the Bern cyclotron laboratory. All electronic devices are located in the physics laboratory [9].

2.3 Experimental set-up

The experimental set-up to perform beam profile measurements is shown in figures 9 and 10. In order to see the effects on the beam due to the Mini Beam Line, one UniBEaM detector is mounted in front and one behind. This whole apparatus is installed on the Beam Transport Line in the beam line bunker. A Faraday cup measures the total beam intensity and stops the beam at the end. The horizontal and vertical alignment is performed using self-leveling lasers (figure 25 in the appendix).
First, the horizontal profile was measured for different quadrupole current settings. Then the two UniBEaM detectors were turned by 90° and vertical profile data were acquired for different quadrupole settings. Afterwards, the steering properties were recorded with only one bending magnet in operation. For this steering measurement, both quadrupole magnets were turned off and vice versa, for the two quadrupole measurements, both steering magnets were switched off. The horizontal steering properties were not tested due to time constraints.

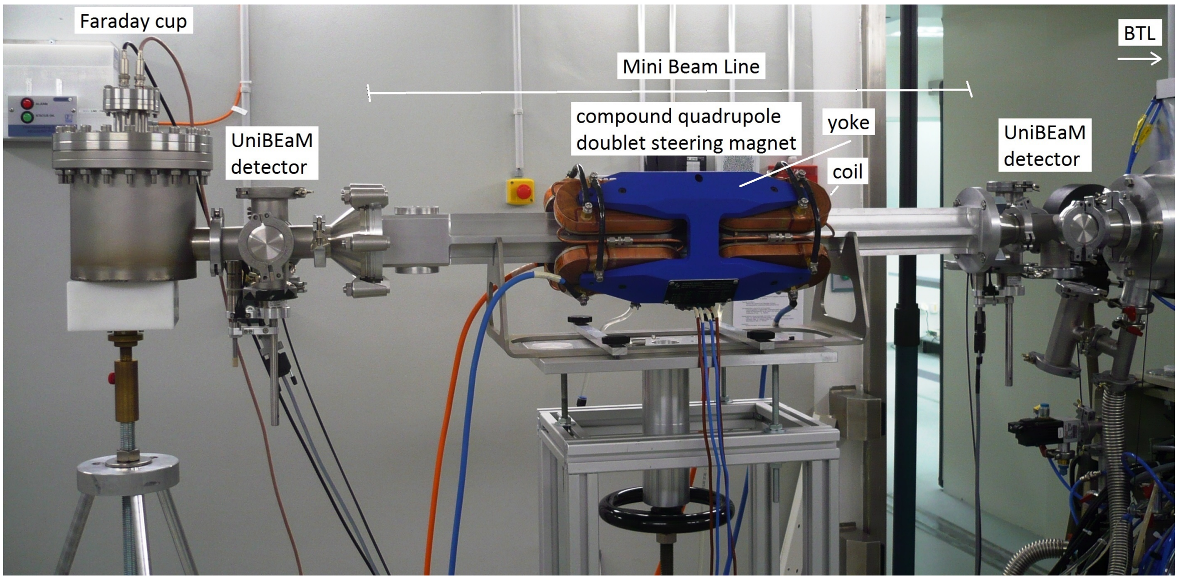

Figure 9: Experimental set-up for performing the beam profile measurements in which all essential elements are indicated.
The UniBEaM detectors are installed in order to measure the vertical profile. A picture made from the other side of the room gives a closer view on the second UniBEaM (figure 10a). The cooling water and current connections to the Mini Beam Line are also visible.

The beam was optimized for the above mentioned three measurement series by the Bern cyclotron group. For the horizontal focusing and defocusing experiment, we wanted to have a wide beam profile on the first UniBEaM detector in order to clearly see the focusing effect on the second UniBEaM. In addition, we wanted to be sure to not over-focus, which is a crossing of the beam inside the transport line and looks like a defocusing when observing the profile on the second UniBEaM. In this way, we checked the correct orientation of the Mini Beam Line. For the focusing and defocusing measurement in the vertical plane, on the contrary, we chose an almost Gaussian beam on UniBEaM 1 and adapted the cyclotron settings slightly in order to minimize beam splitting on the second UniBEaM detector. For the vertical steering measurement, we wanted a tiny beam profile with high intensity on UniBEaM 2 in order to clearly make visible the steering effect.

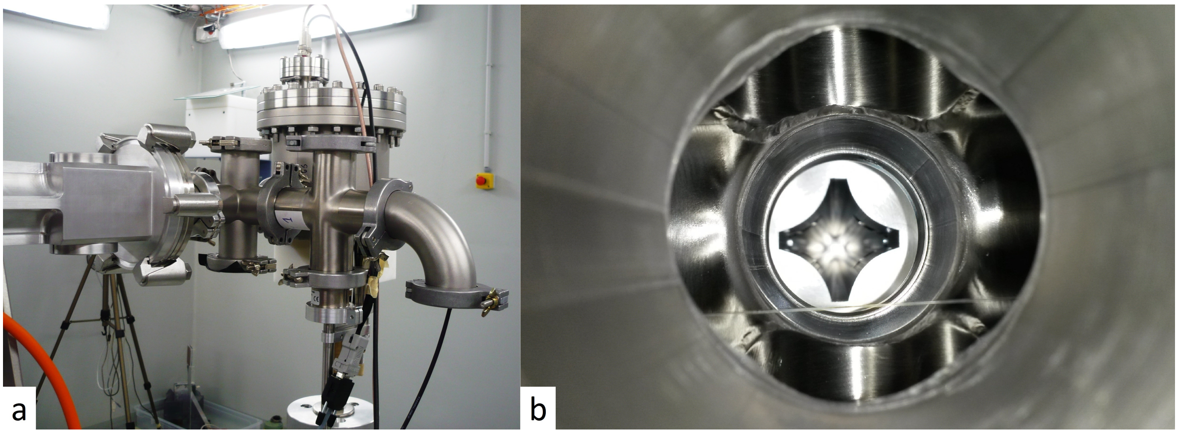

Figure 10: **a)** A closer view to the second UniBEaM from the side. The optical fiber as well as the RS-232 cable connection are visible.
b) Looking through the beam pipe when the Faraday cup has been removed. One can see the horizontal fiber which measures the vertical profile, the branching of the pipes of the UniBEaM detector, the special form of the Mini Beam Line as well as the vacuum tight connection between the first UniBEaM detector and the Beam Transport Line.

Before performing the beam profile measurements, the novel compact beam line was tested on its vacuum tightness. For this purpose, one end of the Mini Beam Line was connected to a turbo molecular pump and a rotary pump in series. The pressure was measured by means of two vacuum gauges embedded in a single instrument (a Pirani type gauge for low vacuum starting from atmospheric pressure down to 10^{-4} mbar and a Penning type gauge for high vacuum with a range of 10^{-3} to 10^{-10} mbar). This combined vacuum gauge was installed at the other end of the beam pipe with respect to the pump in order to measure an upper limit value of the pressure. The vacuum test was performed following the standard procedure described in section 1.5. The results are reported in section 4.1.

3 Simulation of the Mini Beam Line

The Simulation of the Mini Beam Line is performed with the Beamline Simulator, a software developed by D-Pace, and is based on the matrix formalism explained in section 1.4. Using this software, one can define different beam elements as well as apertures in order to have a good visualization of the beam line. In the simulation for this Bachelor thesis, the beam source, the drift space and the quadrupole magnet were used. As we know from the theory, the only parameter in the drift space is its length. For the quadrupole magnet, there is in addition the quadrupole field strength k. It depends on the magnetic field gradient B' in the plane orthogonal to the beam as well as the momentum over charge ratio p/q according to formula 1.6. The p/q ratio is known and the magnetic field gradient B' is approximated with

$$B' = \frac{B_{max}}{r_b} \tag{3.10}$$

where r_b is the bore radius of the magnet [5]. The magnetic field B_{max} can be measured as a function of the current. If we know this function, we can calculate the magnetic field B_{max} out of the current we set on the power supply. This calculation is done later in the chapter in section 3.2.

The Mini Beam Line consists in particular of a compound quadrupole doublet steering magnet. This special beam element is not predefined in the Beamline Simulator. The simulation, therefore takes into account only the quadrupole doublet magnet and neglects the steering function. Figures 11 and 14 illustrate the simulation.

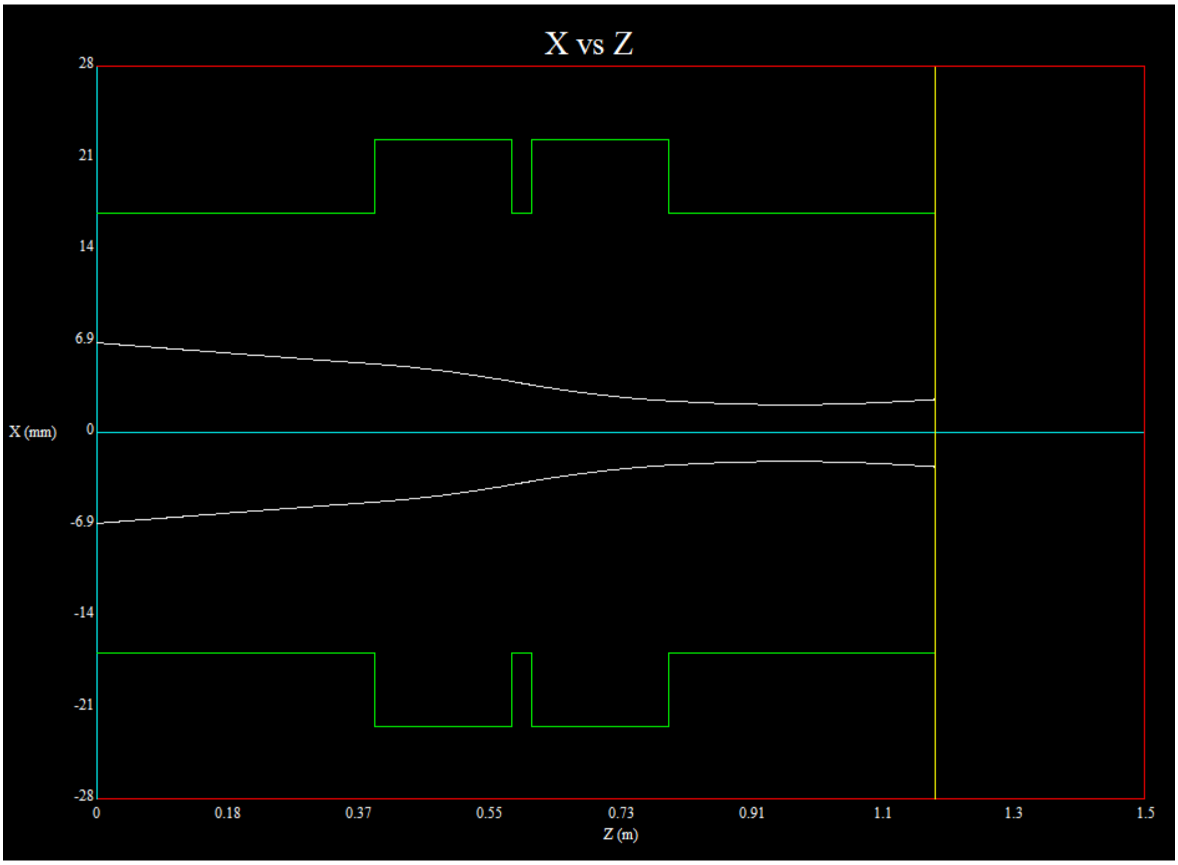

Figure 11: Example of a simulated lateral beam envelope inside the Mini Beam Line for currents of 17 A on quadrupole 1 and 20 A on quadrupole 2 with the beam source parameters of the horizontal focusing and defocusing measurement series (section 3.3).

3.1 Dimensions

In this section, it will be explained how the dimensions of the beam elements were determined. A schematic sketch of the Mini Beam Line with the two UniBEaM detectors is shown in figure 12. The physical as well as the effective lengths are indicated in the figure. The quadrupole lengths have to be corrected because the effective lengths are longer than the iron lengths by half of the bore diameter d_b according to equation 1.7:

$$L \approx \tilde{L} + \frac{1}{2} d_b. \tag{3.11}$$

Because of this, the lengths of the drift spaces also have to be adapted, since the total length of the Mini Beam Line as well as the distance from the fiber in UniBEaM 1 to the fiber in UniBEaM 2 are fixed. Table 3 summarizes the measured physical dimensions as well as the calculated effective lengths.

Since the Mini Beam Line has a special form (visible in figure 10b), the bore diameter is not well-defined. The most reasonable value seams to be the distance from the magnet centreline to the pole tip field. However, this does not correspond to the aperture size.

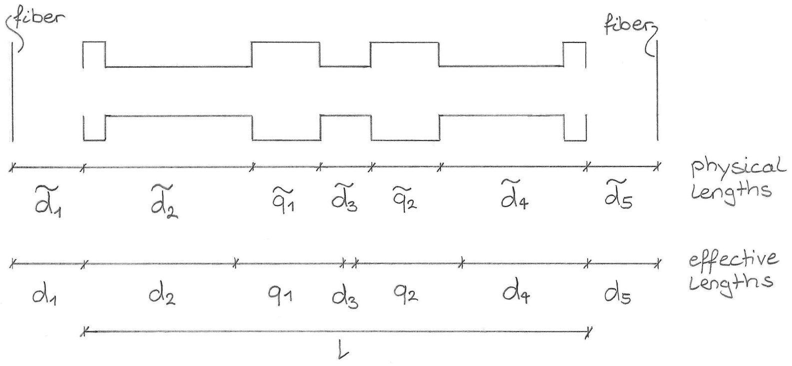

Figure 12: Schematic longitudinal cut of the Mini Beam Line connected to the two UniBEaM detectors with the dimension names indicated.

parameter name	**physical length [mm]**	**parameter name**	**effective length [mm]**
$\tilde{d}_1$	-	d_1	132.00 ± 1.00
$\tilde{d}_2$	-	d_2	256.25 ± 2.20
$\tilde{q}_1$	174 ± 2	q_1	190.50 ± 2.00
$\tilde{d}_3$	45 ± 2	d_3	28.50 ± 2.00
$\tilde{q}_2$	174 ± 2	q_2	190.50 ± 2.00
$\tilde{d}_4$	-	d_4	240.25 ± 2.20
$\tilde{d}_5$	-	d_5	132.00 ± 1.00
l	906.0 ± 0.1*	length of Mini Beam Line	
d_b	33.0 ± 0.3*	bore diameter	
	1170 ± 2	fiber to fiber	
	398 ± 2	first fiber to beginning of front magnet	
	382 ± 2	end of back magnet to second fiber	

Table 3: Dimensions of the Mini Beam Line connected to the two UniBEaM detectors.
The parameter names are the same as in figure 12. The physical lengths were measured directly in the laboratory except for the ones indicated with *, which are taken from the manufacturer of the Mini Beam Line [8]. Out of these, the effective lengths were calculated whereas d_2 and d_4 had, in addition to the bore diameter correction, to be slightly adapted because of the uncertainty of the measurement.

3.2 Quadrupole slope and intercept

The manufacturer of the Mini Beam Line D-PACE measured the magnetic field as a function of the operating current on the quadrupole magnets by means of hall probes. Three measurement series were performed increasing the current from 0 A up to 75 A, decreasing it to zero and increasing it to the maximal operating current again [8, 10, 11]. Out of these data, I did the following calculation. The arithmetic mean of the measured magnetic field values had to be corrected by a factor r_b/r, because the hall probes could not be located at the pole tip field which is $r_b = 16.50 \pm 0.15$ mm away from the symmetry axis of the magnet, but at a closer radius of $r = 15.50 \pm 0.15$ mm due to technical reasons. The absolute value of the resulting magnetic field B_{max} corresponds to the pole tip field strength (table 7 in the appendix). The current as a function of B_{max} was plotted, adding a least squares fit with the straight-line equation

$$I = (\text{slope}) \cdot B_{max} + \text{intercept}. \tag{3.12}$$

This slope and intercept are parameters of the quadrupole beam element to be implemented in the simulation software. Three different methods were applied in order to evaluate these parameters. The method with excel is shown in figures 26a and b in the appendix. However, as excel ignores the errors when performing the least squares fit, a more sophisticated method using ROOT is applied. The plots using this approach are shown in figures 26c and d. As the curve is only linear for low currents, some points were excluded of the fit in order to obtain a χ^2/ndf as close as possible to one. χ^2/ndf is a statistical value which measures the goodness of a fit and is close to one for a good fit. For the first quadrupole, this plot is shown in figure 13 and, for sake of completeness, also in figures 26e and f for both quadrupoles. Table 4 summarizes the results obtained by these three methods and compares them with the data from the manufacturer.

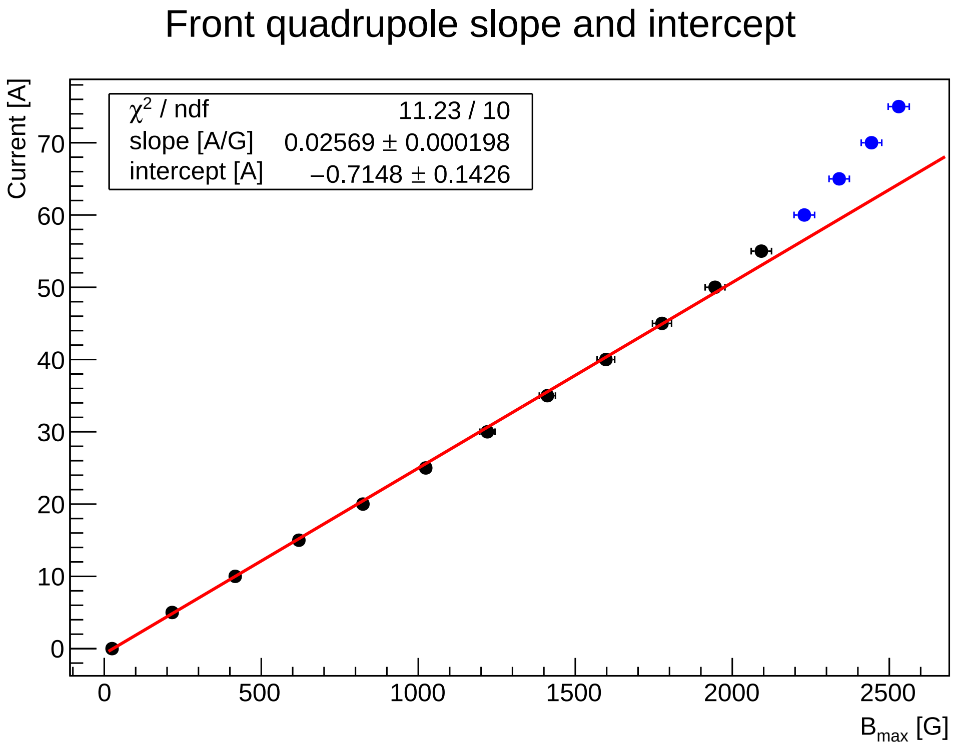

Figure 13: Operating current on the first quadrupole magnet versus the pole tip field B_{max} with a least squares fit. The four blue points are excluded of the fit. The errors in B_{max} come from the standard deviation of average of the three measurement series and are only visible for higher magnetic field values. The current errors are the estimated uncertainty of the ammeter (0.01 A) and are too small to be visible.

The fit with the ROOT data analysis software, where the first 12 points are taken into account, is considered as the best one. However, choosing one or the other fit parameter does not change much the simulation of the Mini Beam Line. Other error sources, like the initial beam matrix, non-linear effects of the Mini Beam Line and the alignment of the experimental

Front quadrupole

Method	slope [A/G]	intercept [A]
ROOT including only 12 points to the fit	0.02569 ± 0.00020	-0.71 ± 0.14
ROOT including all 16 points to the fit	0.02741 ± 0.00016	-1.25 ± 0.15
Excel including all 16 points to the fit	0.0286	-3.1353

Back quadrupole

Method	slope [A/G]	intercept [A]
ROOT including only 12 points to the fit	0.02571 ± 0.00019	-0.72 ± 0.14
ROOT including all 16 points to the fit	0.02726 ± 0.00016	-1.18 ± 0.14
Excel including all 16 points to the fit	0.0286	-3.1114

Front and back quadrupole

	slope [A/G]	intercept [A]
According to the manufacturer D-PACE [8]	0.03030	

Table 4: Fit parameters of the three methods compared with that of the manufacturer where the uncertainties of the excel calculation and the manufacturer's slope value are unknown.

set-up, give larger contributions. A more detailed discussion of the initial beam matrix as well as the non-linear effects of the Mini Beam Line is done in section 4.2.

3.3 Beam source

The Beamline Simulator Software takes the energy of the particles (18 MeV), the mass (930,23 MeV) and the charge (1e) as well as the beam matrix at the point of insertion as an input. The beam matrix can be calculated from the beam emittance ϵ and the Twiss parameters α and β. In a previous experiment, these values have been measured as a function of the cyclotron settings at a certain location along the Beam Transport Line and can now be transported to the location of the first UniBEaM detector.

During the experiment, I noted the cyclotron and Beam Transport Line settings and got the emittance and Twiss parameters delivered from the Bern cyclotron team. Table 5 lists these values for the chosen cyclotron settings, out of whose, the x-component of the beam matrix can be evaluated in the following way

$$\sigma_x = \begin{pmatrix} \epsilon_x \beta_x & -\epsilon_x \alpha_x \\ -\epsilon_x \alpha_x & \epsilon_x \gamma_x \end{pmatrix},$$

where

$$\gamma_x = \frac{1+\alpha_x^2}{\beta_x}. \tag{3.13}$$

The y-component of the beam matrix is calculated in the same way [12].

	Horizontal focusing/defocusing	**Vertical focusing/defocusing**	**Vertical steering**
β_x [m/rad]	3.193759139	0.204907673	10.248444400
α_x	2.014942996	0.503101511	-6.133506378
β_y [m/rad]	0.258386733	1.217303622	9.309374285
α_y	-0.605244580	1.629039212	7.856911355
ϵ_x [mm·mrad]	14.38	14.38	14.38
ϵ_y [mm·mrad]	4.43	4.43	4.43

Table 5: Twiss parameters and transverse beam emittance for the three measurement series corresponding to three different settings of the cyclotron and the long Beam Transport Line.

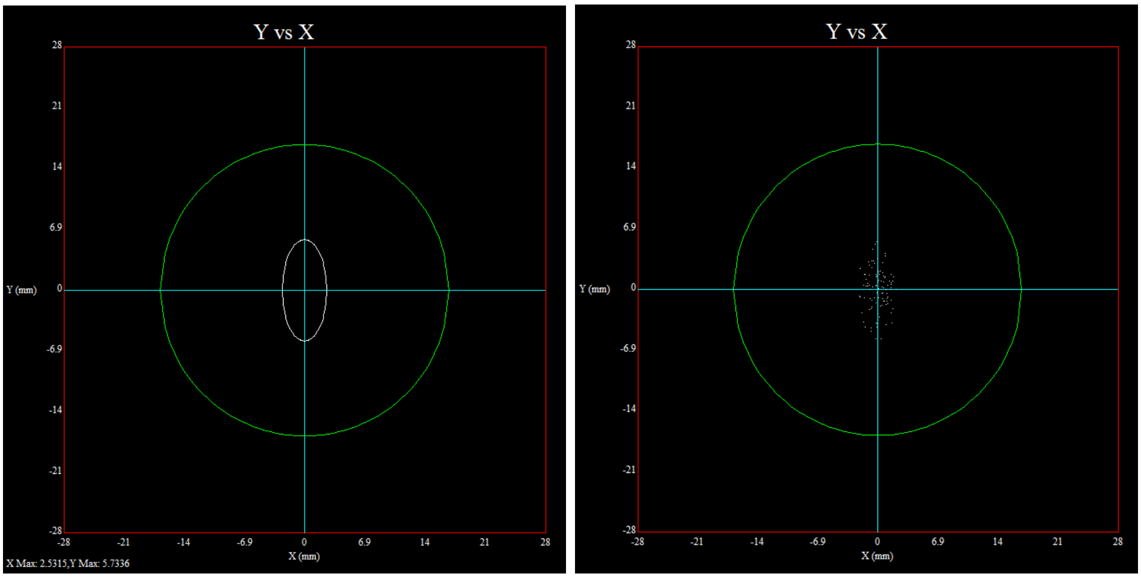

(a) **(b)** 100 particles.

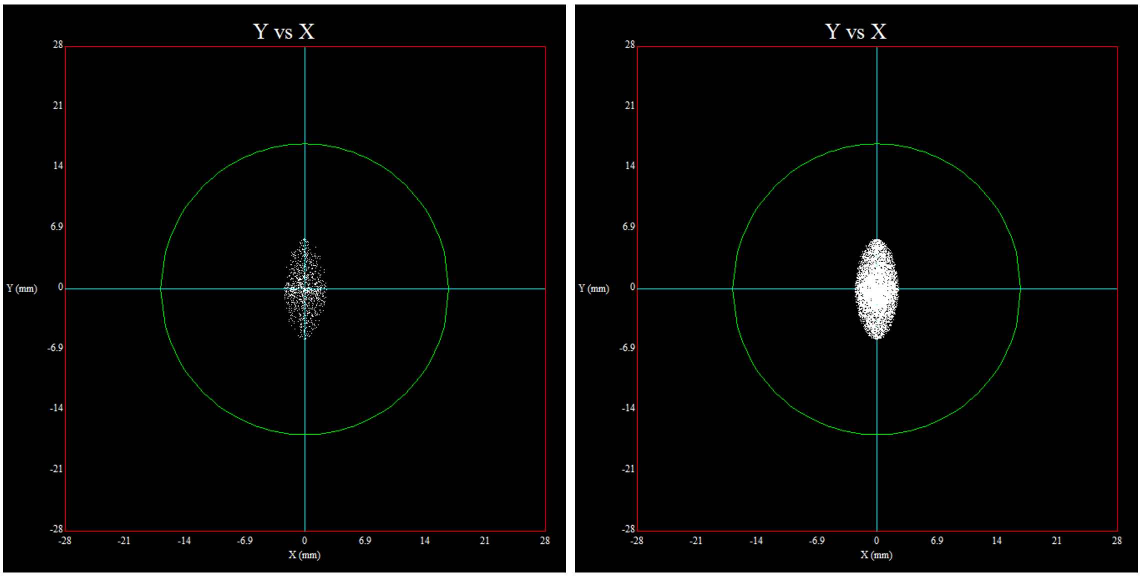

(c) 1’000 particles. **(d)** 10’000 particles.

Figure 14: Simulated transversal beam profiles inside the Mini Beam Line for the same beam and quadrupole settings as in figure 11. Plot a reports the beam envelope, plots b, c, and d are in multi particle mode. The profiles are evaluated at the position of the yellow line in figure 11.

4 Experimental measurements and results

The experimental set-up as well as the procedure for the beam profile measurements is described in section 2.3. Three measurement series were performed, one vertical steering experiment and two focusing/defocusing experiments, one in the horizontal and vertical plane, respectively. The two UniBEaM detectors scanned the beam several times going back and forth with a range of 24 mm, a step size of 0.25 mm and a counting time of 50 ms. For each position, the number of counts was then stored to a text file. Before performing the experiments, the profile scan was done when having no beam in order to evaluate the noise baseline. Since the measured profile data is very reproductive, taking only one run is enough for the evaluation. With a ROOT program, the noise was first subtracted from the measured profiles and afterwards the profile plots could be made. The uncertainties for the number of counts of the preliminary profile and the noise data are set to the square root of the number of counts as it is usually done in statistics. The uncertainty for the number of counts of the final profile is then a combination of the noise and preliminary profile errors. For the uncertainty on the position, half of the step size is taken. With the ROOT program, also profile parameters like the root mean square (RMS), the position of the maximum and the weighted average could be extracted. Before performing profile measurements, a vacuum test was performed.

4.1 Vacuum test

The vacuum test was performed following the standard procedure described in section 1.5 with the experimental set-up explained in section 2.3. The pressure inside the Mini Beam Line was measured over a period of approximately four days. The recorded data are shown in table 8 in the appendix and plotted in figure 15. The pressure uncertainty of the first point is estimated on the basis of pressure fluctuations in the atmosphere and is too small to be visible in the plot. The other pressure uncertainties are set to the half of the last digit on the display of the vacuum gauge. The time uncertainties are due to the time it took to note the data. However, they are only visible for the first few points since it is a logarithmic scale.

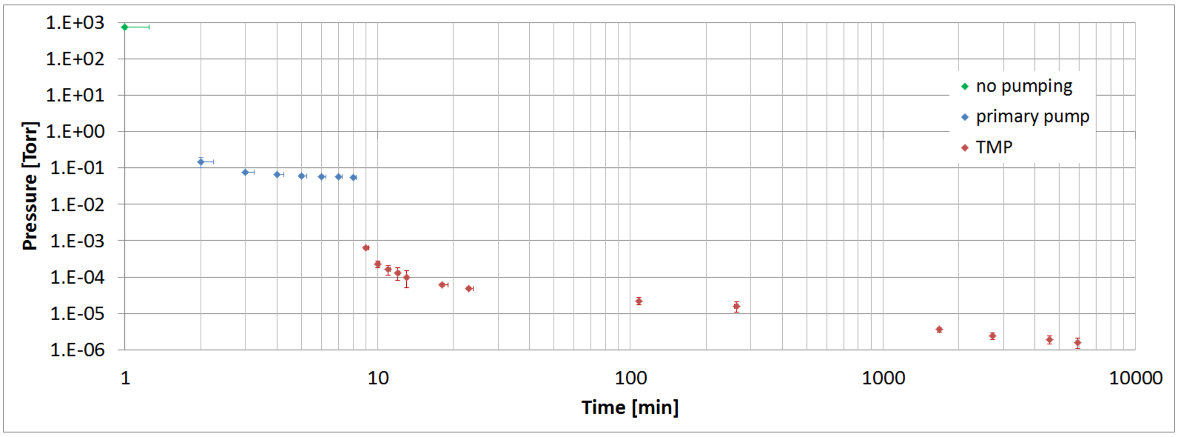

Figure 15: "Pump down" curve.
A log-log plot of the pressure as a function of time where the different pumping systems are marked with different colours. One clearly sees the two steps when turning on the primary pump and the turbo molecular pump, respectively.

Having started the Turbo Molecular Pump (TMP), the pumping system removed slowly degassing humidity sticking at the surfaces. The logarithmic pressure decay is therefore only visible at later stages of the measurement series. That is why the last four points of the pump down curve are plotted on the separate diagram 16.

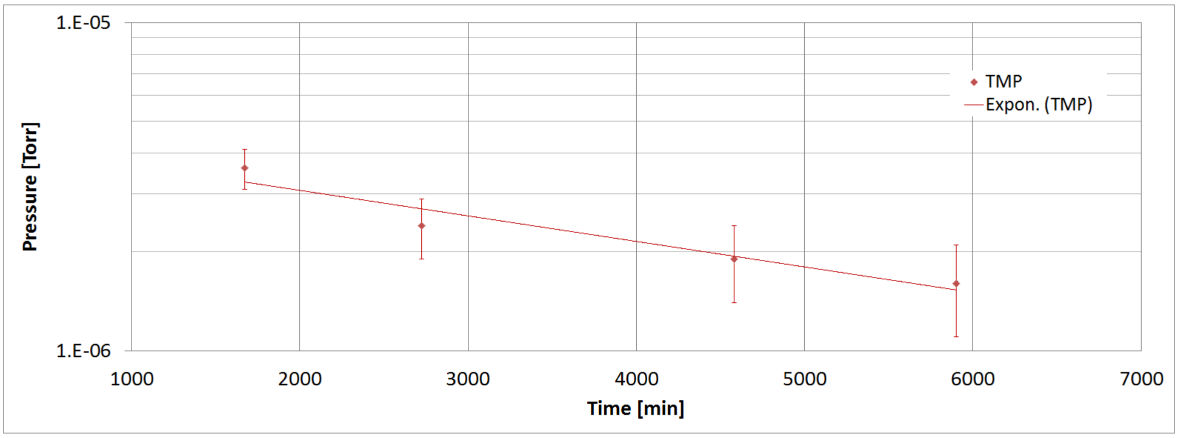

Figure 16: Last four points of pump down curve.
A log-lin diagram of the pressure as a function of the time with an exponential trend line. The four points are aligned.

As expected, there is a clear step when changing the technology (figure 15) and the pressure as a function of the time follows the logarithmic decay law (figure 16). The vacuum obtained is $1.6 \cdot 10^{-6}$ Torr which is a good value for the purposes of this thesis. This means that there are no leaks and or virtual leaks (air inclusions, e.g. in a screw, which comes out at some time of the pumping process and deteriorates the vacuum). Thus, the test was successful.

4.2 Focusing and defocusing

With the orientation of the Mini Beam Line shown in figure 9, the focusing and defocusing effects correspond qualitatively to the predictions. Figure 17 visualizes the focusing effect.

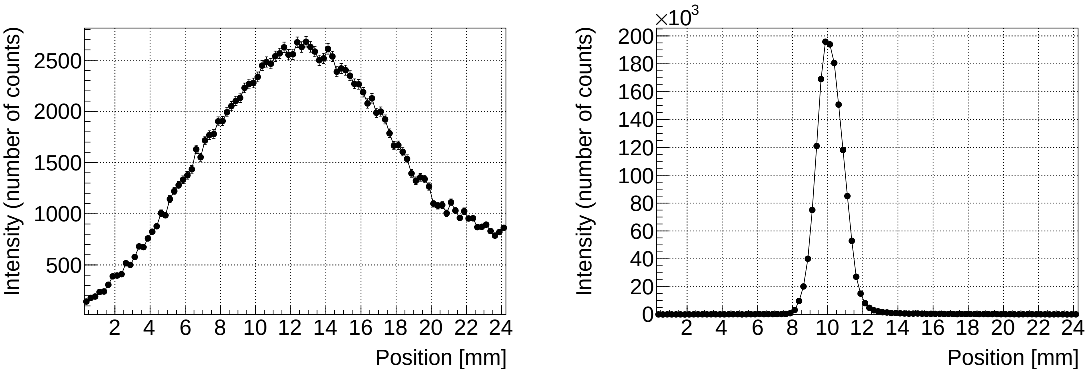

(a) Profile on UniBEaM 1.

(b) Profile on UniBEaM 2.

Figure 17: Focusing in the horizontal plane with 30 A on the first and 20 A on the second quadrupole magnet.

The focusing and defocusing measurements were recorded in the horizontal and vertical plane separately. Three sub-measurement series were performed for each plane, fixing the current on one quadrupole magnet and varying it on the other one. Table 9 in the appendix lists the current settings as well as the RMS on the two beam profilers. The RMS is a statistical measure for the width of a profile. The smaller it is, the better focused the beam is at the corresponding position along the beam line. Colours in table 9 as well as in the following figures help to keep the overview of the totally six sub-measurement series.

In the laboratory, focusing and defocusing effects in both planes could be observed, but focusing in the vertical direction needed much higher currents in order to reach the same effects as in the horizontal plane. This is due to the different initial beams. In the horizontal plane, the beam was slightly converging when entering the Mini Beam Line. In the vertical plane, on the contrary, the beam was converging so much when passing UniBEaM 1 that it crossed inside the Mini Beam Line, which made focusing much more difficult. In the horizontal plane, the following could be observed: Increasing the current stepwise on the first quadrupole magnet and having it fixed on the other magnet, a wide profile on UniBEaM 2 which became narrower and narrower and finally reached a minimum width could be seen. Afterwards, the profile became wider again. A typical example of this beam development is given in figure 18. This waist point in the profile width was, however, not observed in the vertical plane, because the power supply could not provide higher currents. The development of the beam profile on the second UniBEaM is reported for each of the totally six sub-measurement series in figures 27 and 28 in the appendix.

The two plots in figure 19 show the focusing and defocusing effects on the second UniBEaM detector in both planes as a function of the current on the first quadrupole magnet (Q_1) for different current settings on the second quadrupole (Q_2) - figure 19a - and vice versa (figure 19b). Figure 20 is done with the same data as figure 19b, but the plotted RMS is normalized to the RMS of the profile with no current on Q_2.

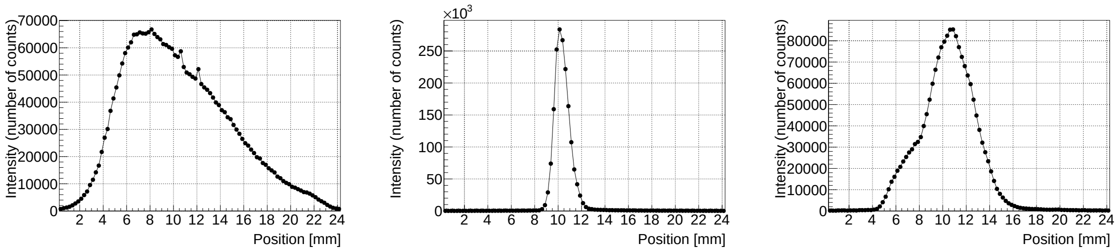

(a) Q_1 turned off. **(b)** 20 A on Q_1. **(c)** 30 A on Q_1.

Figure 18: Horizontal beam profile development on UniBEaM 2 with Q_2 turned off (marked in blue in table 9 and figures 19, 21, 27 and 29).

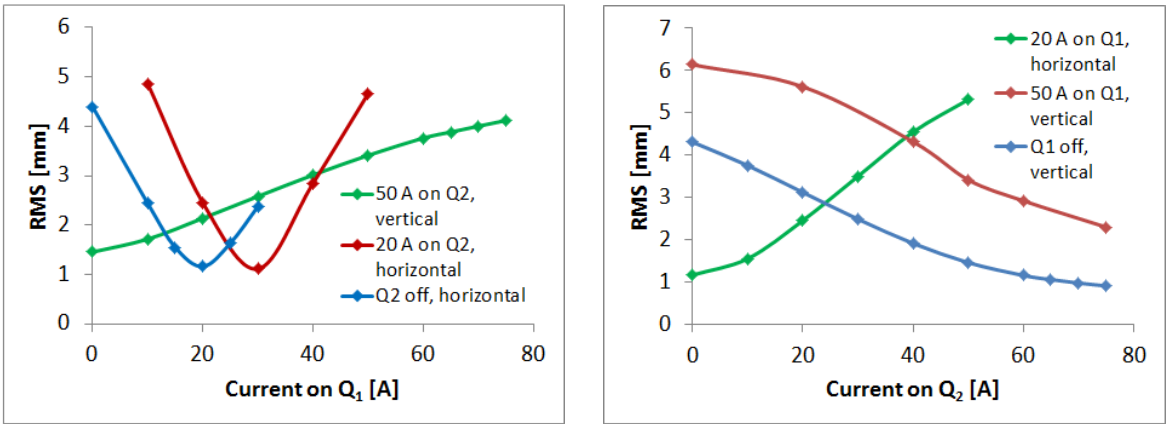

(a) The waist points of the horizontal measurements - profiles with minimal RMS - in the blue and red lines are clearly visible.

(b) There are no waist points in the vertical measurement series.

Figure 19: Focusing and defocusing effects in both planes.
Focusing in one plane means defocusing in the other plane, which corresponds to the theory.

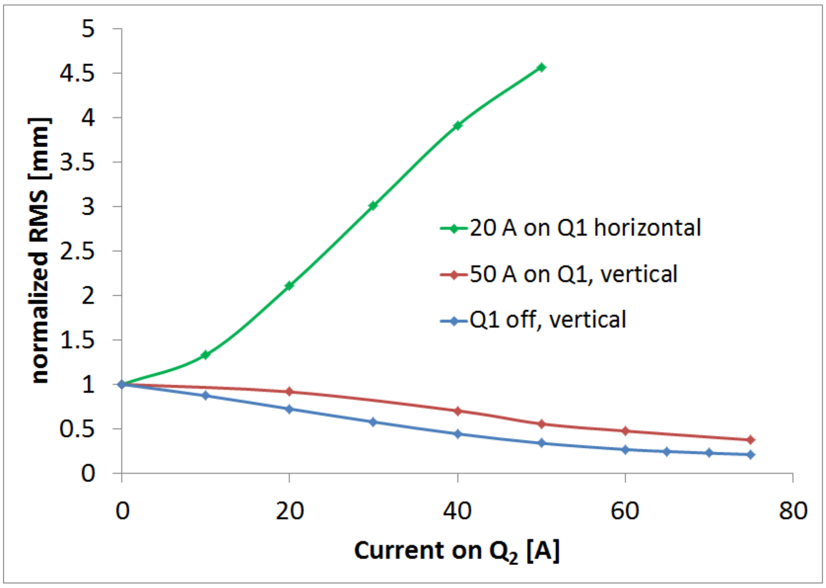

Figure 20: Focusing and defocusing effects in both planes.

The simulation assumes always a Gaussian beam [5], while in reality, the beam extracted from the cyclotron is not Gaussian. A direct comparison of RMS values obtained in the experiment and the simulation, therefore, makes no sense. In order to circumvent this problem, the experimental RMS on UniBEaM 2 was divided by the experimental RMS on UniBEaM 1 and this "focusing ratio" was compared to the one obtained in the simulation. A focusing ratio greater than 1 means defocusing while less than 1 means focusing. The smaller the ratio is, the more the beam gets focused. The simulated focusing ratio is calculated from the beam envelope's maximum values at the position of UniBEaM 1 and 2. These maximal values are reported in table 9 in the appendix. Plotting the focusing ratio as a function of the varied current, one can compare the measurement to the simulation. Figure 21 shows this comparison for the horizontal sub-measurement series, where Q_2 was turned off (blue line of plot 19a). On the whole, the shape of the two curves are similar. However, the numerical values differ up to a factor two. The waist point - minimal width of profile - is at a higher current on Q_1 for the measurement as for the simulation curve. This curve shifting is probably because the initial beam parameters of the simulation do not coincide with reality. The beam emittance and Twiss parameters were measured during a previous experiment for similar beam settings, but not during this experiment with the actually chosen cyclotron settings. Even if the beam emittance was the same, the Twiss parameters could be different due to other cyclotron conditions. Figure 22 shows the comparison of the experiment to the simulation for the vertical sub-measurement series with 50 A on Q_1 (red curve of plot 19b). In addition to the shifting, there is a little shape difference in the two curves which is probably due to non-linear effects of the Mini Beam Line. These non-linear effects are not taken into account by the simulation, because the Beamline Simulator considers all beam elements as separated items without overlapping fields [5]. In reality, however, the two quadrupole magnets are so close to each other and additionally share a single yoke that changing the current on one will affect the magnetic field of the other one [8]. The study of these effects goes beyond the scope of this thesis. My work triggered further developments that are now ongoing at the Bern cyclotron laboratory. Similarly to figures 21 and 22, also the other lines of the two plots in figure 19 are compared to the simulation (figure 29 in the appendix).

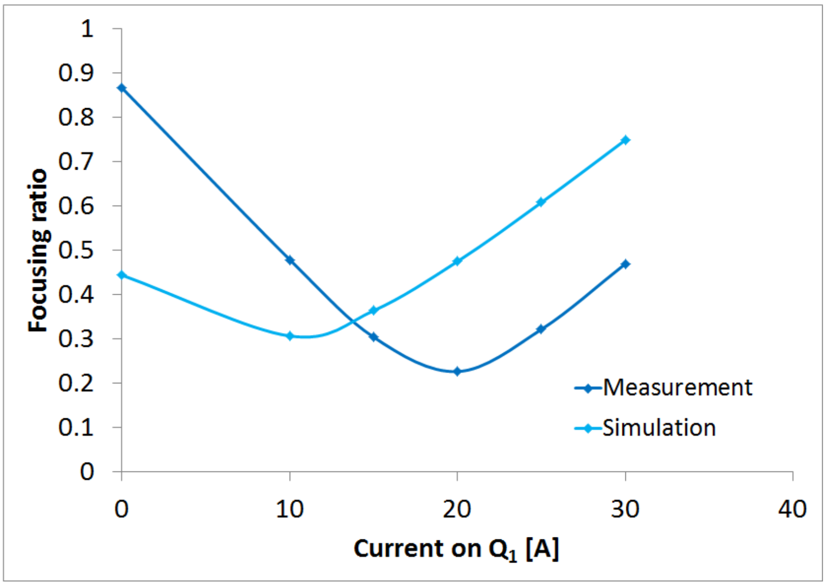

Figure 21: Comparison of measurement and simulation for the blue curve in figure 19a (Q_2 turned off, horizontal profiles).

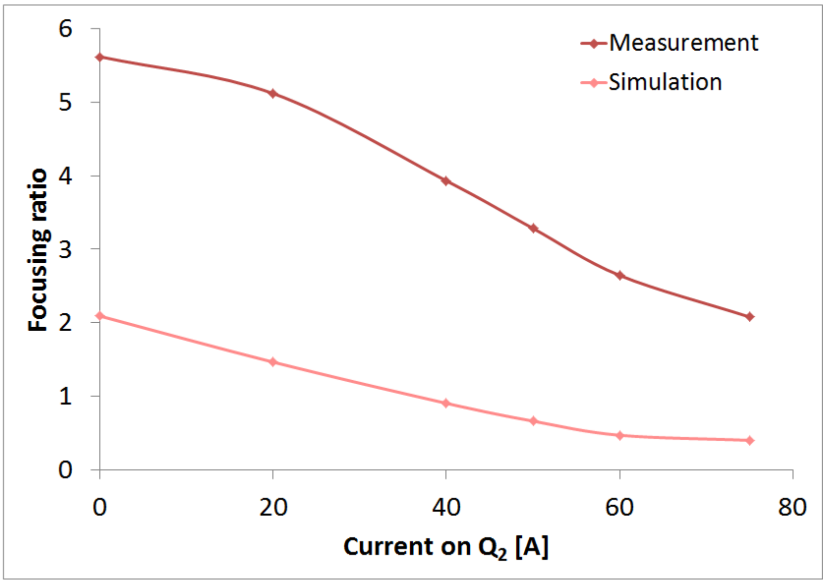

Figure 22: Comparison of measurement and simulation for the red curve in figure 19b (50 A on Q_1, vertical profiles).

4.3 Steering

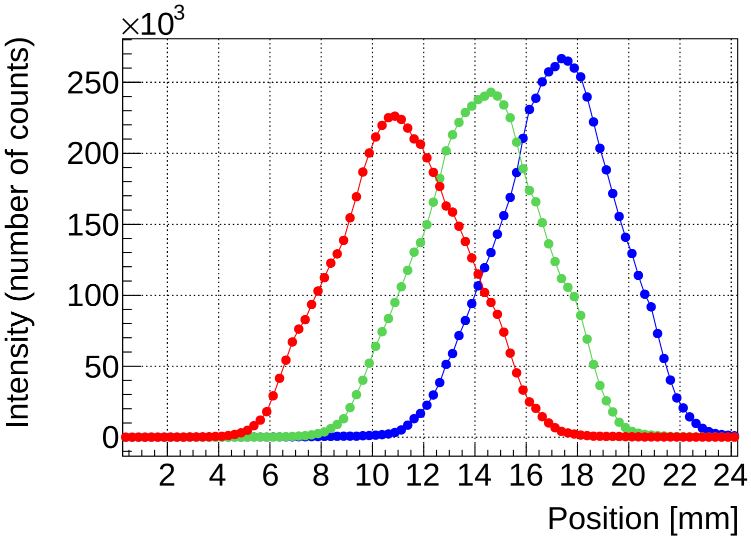

Figure 23: Vertical beam profiles on the second UniBEaM detector for currents of -10 A (red), 0 A (green) and 10 A (blue) on the vertical steering magnet. Changes in the profile shape are visible.

The vertical steering effect is visualized in figure 23. The measurement showed that the vertical steering magnet operates linearly with respect to its operating current (figure 24) and the maximal achieved steering angle is measured to be

$$\text{Maximum steering angle} = (3.91 \pm 0.23)\ \text{mrad}. \tag{4.14}$$

The vertical beam profiles were recorded for five current settings covering the whole range of the power supply. This set of profiles on the second UniBEaM detector is shown in figure 30

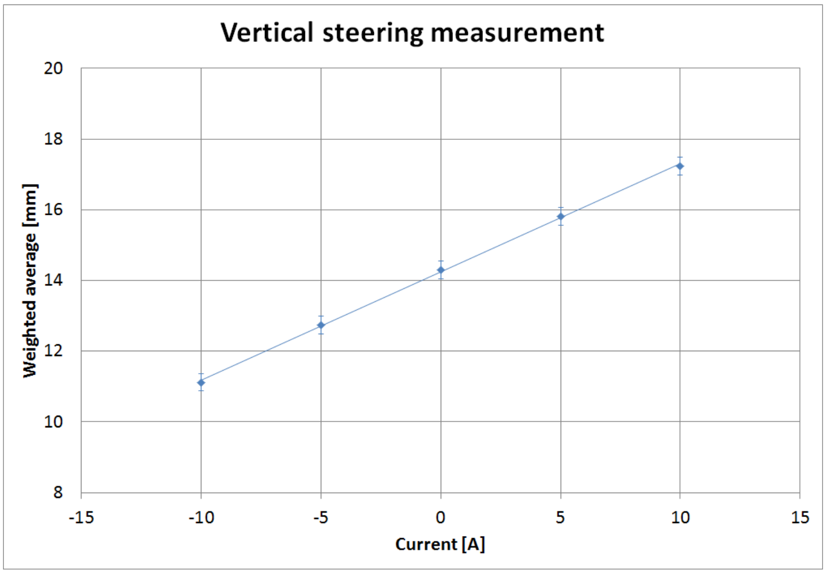

Figure 24: Linear dependence of the beam profile's position with respect to the current for the vertical steering measurement series. The position of the beam is evaluated by means of the weighted average of the profile.

in the appendix. The weighted average, which corresponds to the position of the maximum for a Gauss curve, is one of the profile parameters extracted with the ROOT program. Its values for the different current settings are listed in table 6 and plotted in figure 24.
The position of the maximum as a function of the current was also plotted. The linear dependence was visible but not as exact as for the weighted average because the profiles have a small asymmetry. Through the bending, this asymmetry is modified (figures 23 and 30), which causes the non-linear behaviour of the position of the maximum. The weighted average, on the contrary, is not affected by the asymmetry change of the profile.

Profile number	**Current [A]**	**Weighted average [mm]**
1	10	17.23 ± 0.25
2	5	15.81 ± 0.25
3	0	14.29 ± 0.25
4	-5	12.73 ± 0.25
5	-10	11.12 ± 0.25
Largest position difference		6.1 ± 0.4

Table 6: Steering measurement results.
The uncertainties of the weighted average are assumed to be the step size of the UniBEaM detector and the ones of the current are unknown.

The maximum steering angle is calculated out of the largest position difference of the profile's weighted averages divided by two and the distance from the beginning of the first magnet to the second UniBEaM detector (781.8 ± 2.8 mm effective length). The latter is obtained using table 3.

Comparing these results with the specifications from D-PACE, the linear bending function of the vertical steering magnet with its operating current could be validated. The maximal achieved steering angle is smaller by a factor 5/3 because the Bern medical cyclotron operates with 18 MeV protons and not with 12.6 MeV protons, as it is specified by D-PACE (section 2.1). As already stated in section 2.3, the horizontal steering properties of the Mini Beam Line were not tested due to time constraints. Very similar effects are expected.

5 Conclusions and outlook

A novel compact Mini Beam Line designed for medical cyclotrons was successfully installed and tested for the first time at the Bern cyclotron laboratory.

The vacuum test was successful which means that there are no leaks and or virtual leaks in the Mini Beam Line. The focusing and defocusing effects correspond qualitatively to the simulation but not quantitatively. The most important reasons for this deviation are mainly the beam source parameters implemented in the simulation, which were obtained from a previous experiment and not measured online, as well as the non-linear effects of the Mini Beam Line. The linear bending function of the vertical steering magnet with its operating current could be validated and the maximal steering angle was measured to be (3.91 ± 0.23) mrad.

Overall, this Bachelor thesis shows that the focusing and defocusing as well as the steering properties of the novel compact beam line work well. First qualitative and quantitative results were obtained.

This work served as the basis for further developments. In particular, the power supplies were upgraded to improve the performance at 18 MeV. More complex studies on the properties and simulation of the Mini Beam Line are ongoing aimed at irradiating the target flat and at the right position for an optimized radioisotope production.

Acknowledgements

I wish to warmly thank my supervisor, PD Dr. Saverio Braccini, for the advice and structured guidance he has provided throughout my work. I have been extremely lucky to have a supervisor who cared so much about my work, and who responded to my questions and queries so promptly. You were an excellent mentor!

I would also like to thank Konrad Nesteruk for the helpful tips and feedback he gave me during my work. He helped me performing the simulation as well as the data analysis with ROOT and like this, I could acquire new computer skills.

Together with Maria Antonietta Gilio, who works on the Mini Beam Line for her Master thesis, and Tommaso Carzaniga, we all together were a good team in the laboratory and I could ask questions at any time during my work.

Finally, I wish to thank Jonathan Gasser who carefully read through my thesis, gave me a very detailed feedback in order to ensure an unequivocally phrasing and made me attentive on linguistic errors. I would also like to thank Yves Bandi who read part of my thesis and gave me some stylistic as well as linguistic feedback.

References

[1] E. O. Lawrence and M. S. Livingston, The Production of High Speed Protons without the use of High Voltages, Phys. Rev. 38 (1931) 834.

[2] E. O. Lawrence and M. S. Livingston, The Production of High Speed Light Ions without the Use of High Voltages, Phys. Rev. 40 (1932) 19 35.

[3] S. Braccini, Particle Accelerators and Detectors for medical Diagnostics and Therapy, Habilitation thesis, University of Bern, 2013, arXiv:1601.06820 [physics.med-ph].

[4] H. Wiedemann, Particle Accelerator Physics ed. 3, Springer-Verlag Berlin Heidelberg, 2007.

[5] K. Dehnel and M. Dehnel, Using Beamline Simulator v. 1.3, published by AccelSoft Inc., Del Mar (CA), USA, 1998.

[6] K. P. Nesteruk, M. Auger, S. Braccini, T. S. Carzaniga, A. Ereditato and P. Scampoli, Study of the transverse beam emittance of the Bern medical cyclotron, International Beam Instrumentation Conference (IBIC2015), Melbourne, Australia, September 2015, MOPB041, pp. 134-138.

[7] www.d-pace.com [as at 6th July 2016].

[8] P. Jackle, User manual Mini-PET Beamline v. 1.1, published by Dehnel – Particle Accelerator Components and Engineering Inc., Nelson (BC), Canada, 2015.

[9] M. Auger, S. Braccini, T. S. Carzaniga, A. Ereditato, K. P. Nesteruk and P. Scampoli, A detector based on silica fibers for ion beam monitoring in a wide current range, Journal of Instrumentation 11 (2016) P03027.

[10] P. Jackle, Factory acceptance test for Mini-PET Beamline steerer/quadrupole doublet (1800429), published by Dehnel – Particle Accelerator Components and Engineering Inc., Nelson (BC), Canada, 2014.

[11] P. Jackle, Mini-PET Magnet Characterization, published by Dehnel – Particle Accelerator Components and Engineering Inc., Nelson (BC), Canada, 2014.

[12] P. Forck, Lecture Notes on Beam Instrumentation and Diagnostics, Joint University Accelerator School (JUAS), Darmstadt, Germany, 2011.

Appendix

Experimental set-up

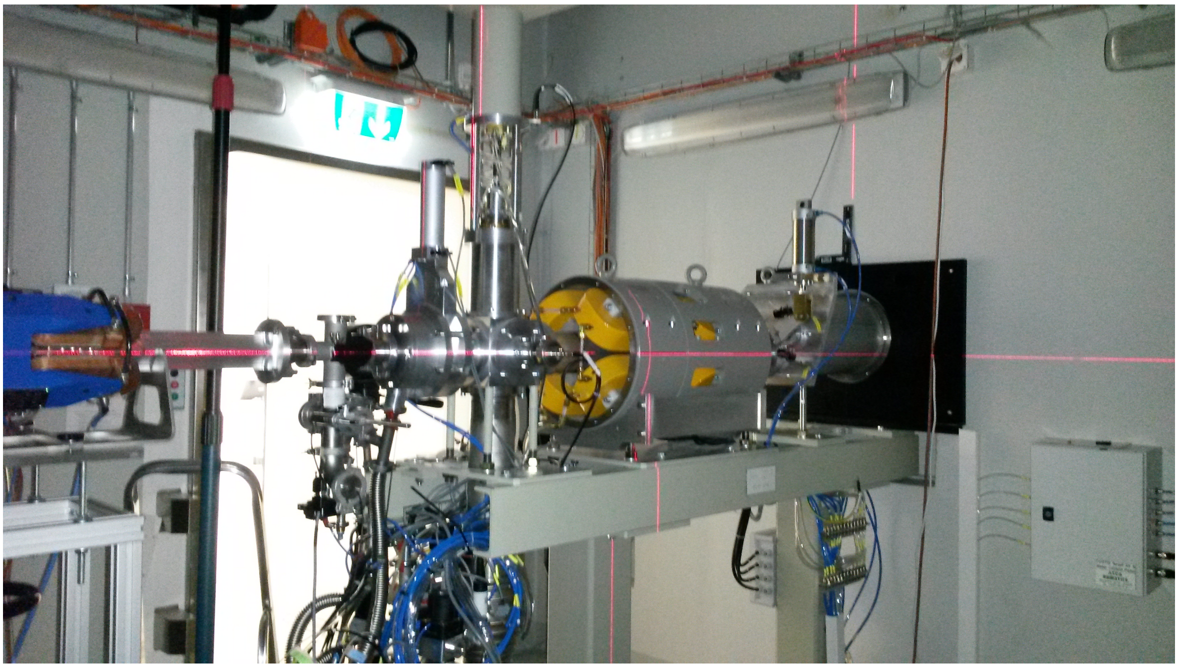

Figure 25: Alignment of the experimental set-up using self-leveling lasers (not yet in focus on the figure).

Quadrupole slope and intercept

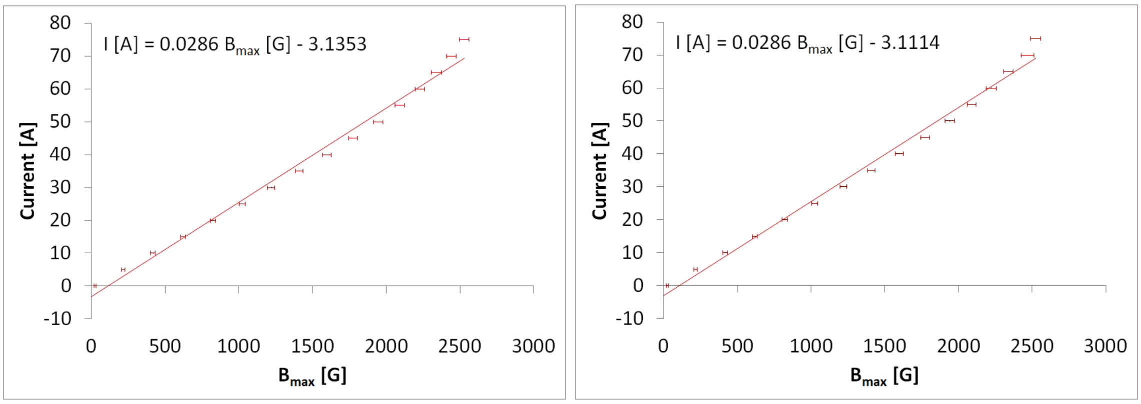

(a) Including all 16 points to the fit (Excel). **(b)** Including all 16 points to the fit (Excel).

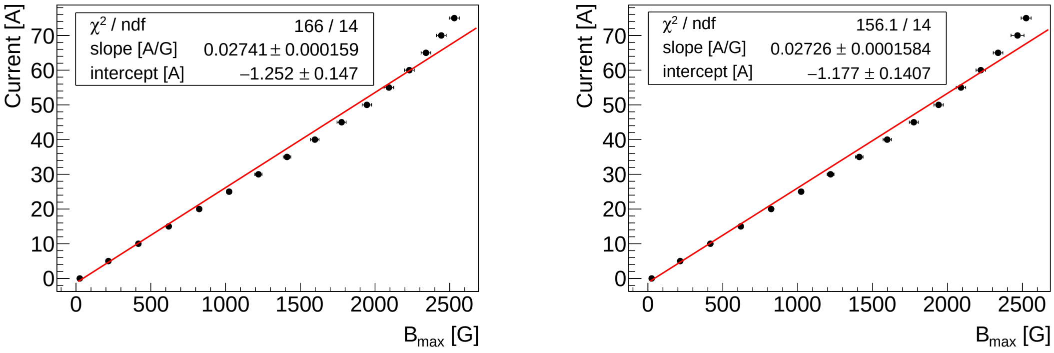

(c) Including all 16 points to the fit (ROOT). **(d)** Including all 16 points to the fit (ROOT).

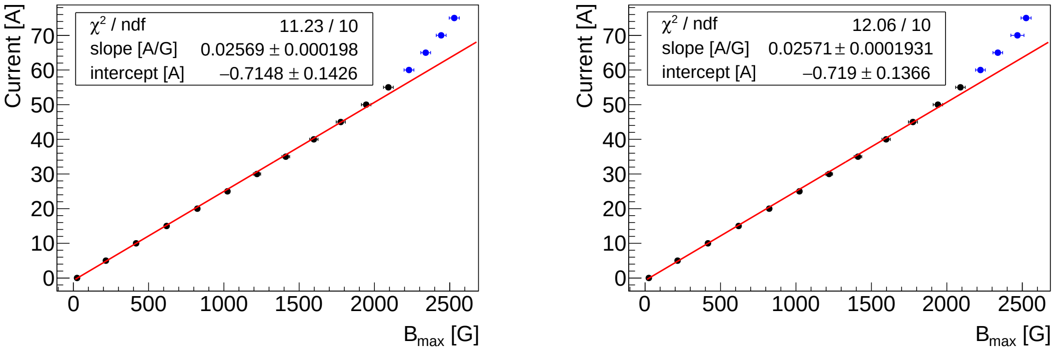

(e) Including 12 points to the fit (ROOT). **(f)** Including 12 points to the fit (ROOT).

Figure 26: The same as figure 13 for the front (left) and back (right) quadrupole magnet including 12 or 16 points to the fit using one of the two programs ROOT or Excel.

Front quadrupole magnet							
	0 to 75 A	75 to 0 A	0 to 75 A	Arithmetic mean	Standard deviation of the average	Corrected value	Error
I [A]*	B_1 [G]*	B_1 [G]*	B_1 [G]*	B_1 [G]	B_1 [G]	B_{max} [G]	B_{max} [G]
0.00	-11.1	-29.4	-29.4	-23.3	6.1	25	7
5.00	-188.5	-222.6	-198.3	-203.1	10.1	216	11
10.00	-375.6	-417.4	-382.1	-391.7	13.0	417	15
15.00	-566.0	-608.5	-572.2	-582.2	13.3	620	16
20.00	-758.2	-800.9	-762.5	-773.9	13.6	824	18
25.00	-945.2	-990.4	-949.8	-961.8	14.4	1024	20
30.00	-1127.2	-1179.7	-1131.6	-1146.2	16.8	1220	24
35.00	-1306.9	-1358.6	-1311.4	-1325.6	16.5	1411	26
40.00	-1481.6	-1534.9	-1485.6	-1500.7	17.1	1598	28
45.00	-1648.6	-1704.5	-1652.6	-1668.6	18.0	1776	30
50.00	-1811.4	-1861.1	-1809.2	-1827.2	16.9	1945	32
55.00	-1949.4	-1997.0	-1951.0	-1965.8	15.6	2093	32
60.00	-2084.1	-2120.7	-2078.2	-2094.3	13.3	2229	33
65.00	-2191.2	-2215.8	-2189.0	-2198.7	8.6	2341	32
70.00	-2289.2	-2302.6	-2293.9	-2295.2	3.9	2443	33
75.00	-2377.3	-2377.3	-2375.6	-2376.7	0.6	2530	34

Back quadrupole magnet							
	0 to 75 A	75 to 0 A	0 to 75 A	Arithmetic mean	Standard deviation of the average	Corrected value	Error
I [A]*	B_2 [G]*	B_2 [G]*	B_2 [G]*	B_2 [G]	B_2 [G]	B_{max} [G]	B_{max} [G]
0.00	12.2	29.3	29.3	23.6	5.7	25	6
5.00	186.4	222.7	198.7	202.6	10.7	216	12
10.00	375.4	416.0	383.4	391.6	12.4	417	14
15.00	566.3	608.7	572.9	582.6	13.2	620	16
20.00	755.8	800.8	762.9	773.2	14.0	823	18
25.00	944.0	989.9	949.6	961.2	14.5	1023	21
30.00	1128.6	1176.0	1132.4	1145.7	15.2	1220	23
35.00	1307.7	1357.5	1311.7	1325.6	16.0	1411	25
40.00	1482.8	1534.3	1485.4	1500.8	16.8	1598	28
45.00	1648.7	1701.9	1652.0	1667.5	17.2	1775	30
50.00	1805.7	1856.1	1807.4	1823.1	16.5	1941	31
55.00	1948.3	1992.6	1949.3	1963.4	14.6	2090	32
60.00	2074.8	2112.0	2077.2	2088.0	12.0	2223	32
65.00	2188.0	2212.0	2188.1	2196.0	8.0	2338	32
70.00	2285.2	2298.0	2371.3	2318.2	26.8	2468	43
75.00	2372.6	2372.4	2371.3	2372.1	0.4	2525	34

Table 7: Calculation of B_{max} out of the measured magnetic field B_1 and B_2 in the front and back quadrupole magnet respectively according to the explanation in section 3.2. The data indicated with * is taken from [8]. The error of B_{max} is obtained by error propagation where the uncertainties of the distances from the magnet centreline r_b and r are estimated to be 0.15 mm (on the basis of the uncertainty of the bore diameter in [8]).

Vacuum test

p [Torr]	**s_p [Torr]**	**t [min]**	**s_t [min] (positive)**	**s_t [min] (negative)**	**remark**
1 atm = 760 Torr	90	1.000	0.250	0.017	start primary pump
1.5E-01	5.E-02	2.000	0.250	0.017	
7.5E-02	5.E-03	3.000	0.250	0.017	
6.5E-02	5.E-03	4.000	0.250	0.017	
6.1E-02	5.E-03	5.000	0.250	0.017	
5.9E-02	5.E-03	6.000	0.250	0.017	
5.7E-02	5.E-03	7.000	0.250	0.017	
5.6E-02	5.E-03	8.000	0.250	0.017	start TMP
6.4E-04	5.E-05	9.000	0.250	0.017	TMP at 450 Hz rotation frequency, increasing
2.3E-04	5.E-05	10.000	0.250	0.017	TMP at 850 Hz rotation frequency, increasing
1.6E-04	5.E-05	11.000	0.250	0.017	TMP at nominal rotation frequency (1000 Hz)
1.3E-04	5.E-05	12.000	0.250	0.017	
1.0E-04	5.E-05	13.000	0.250	0.017	
6.1E-05	5.E-06	18.000	1.000	0.017	
4.8E-05	5.E-06	23.000	1.000	0.017	
2.2E-05	5.E-06	108.000	1.000	0.017	
1.6E-05	5.E-06	263	5	5	
3.6E-06	5.E-07	1673	5	5	
2.4E-06	5.E-07	2723	5	5	
1.9E-06	5.E-07	4583	5	5	
1.6E-06	5.E-07	5903	5	5	

Table 8: Pump down curve data (pressure p as a function of the time t together with their uncertainties s).

Focusing and defocusing

Horizontal profile measurement

I on Q_1 [A]	I on Q_2 [A]	RMS UniBEaM 1 (measured)	RMS UniBEaM 2 (measured)	x_{max} UniBEaM 1 (simulation 12)	x_{max} UniBEaM 2 (simulation 12)
0	0*	5.07621	4.39764	6.7769	3.0081
10	0	5.09985	2.44212	6.7769	2.0779
15	0	5.09116	1.54811	6.7796	2.4668
20*	0*	5.13327	1.16184	6.7796	3.2191
25	0	5.09304	1.63731	6.7769	4.1201
30	0*	5.06927	2.37934	6.7769	5.0749
20	10	5.06827	1.54889	6.7769	2.7869
20*	20	5.11585	2.45139	6.7769	2.6104
20	30	5.14287	3.49725	6.7796	2.7850
20	40	5.16708	4.54456	6.7769	3.2961
20*	50	5.17957	5.30992	6.7769	4.0531
10	20*	5.25027	4.86183	6.7796	3.2964
30	20*	5.27777	1.11354	6.7769	4.1635
40	20	5.30380	2.84931	6.7769	6.3638
50	20*	5.35279	4.66561	6.7796	8.6322

Vertical profile measurement

I on Q_1 [A]	I on Q_2 [A]	RMS UniBEaM 1 (measured)	RMS UniBEaM 2 (measured)	y_{max} UniBEaM 1 (simulation 12)	y_{max} UniBEaM 2 (simulation 12)
0*	0	0.98663	4.30576	2.3222	2.5768
0	10	1.00969	3.75316	2.3222	2.2347
0	20	1.00842	3.11648	2.3222	1.9460
0	30	1.00737	2.48395	2.3222	1.7241
0*	40	1.00728	1.91067	2.3222	1.5834
0	50*	1.01195	1.45624	2.3222	1.5333
0	60	1.02245	1.15392	2.3222	1.5703
0	65	1.01328	1.05399	2.3222	1.6167
0	70	1.02200	0.97314	2.3222	1.6782
0*	75	1.01863	0.90407	2.3222	1.7522
10	50	1.02464	1.71715	2.3222	1.3760
20	50	1.02774	2.14063	2.3222	1.2772
30	50	1.03828	2.58256	2.3222	1.2640
40	50*	1.02776	3.01577	2.3222	1.3525
50	50	1.03966	3.41349	2.3222	1.5376
60	50	1.04758	3.76104	2.3222	1.8013
65	50	1.05504	3.88378	2.3222	1.9567
70	50	1.05895	4.00356	2.3222	2.1251
75	50*	1.05691	4.11843	2.3222	2.3050
0	0	1.07101	4.50817	2.3222	2.5768
50*	0	1.09220	6.13713	2.3222	4.8574
50	20	1.09732	5.61727	2.3222	3.4014
50*	40	1.09813	4.31563	2.3222	2.1007
50	60	1.10369	2.91819	2.3222	1.0917
50*	75	1.10522	2.29690	2.3222	0.9288

Table 9: Current settings, experimental RMS and beam envelope's maximum values of the simulation - using the quadrupole slope obtained by including 12 points to the fit (section 3.2) - for the horizontal and vertical quadrupole measurement series. The sub-measurement series are made visible with colours. The * indicates the printed profiles on figures 27 and 28.

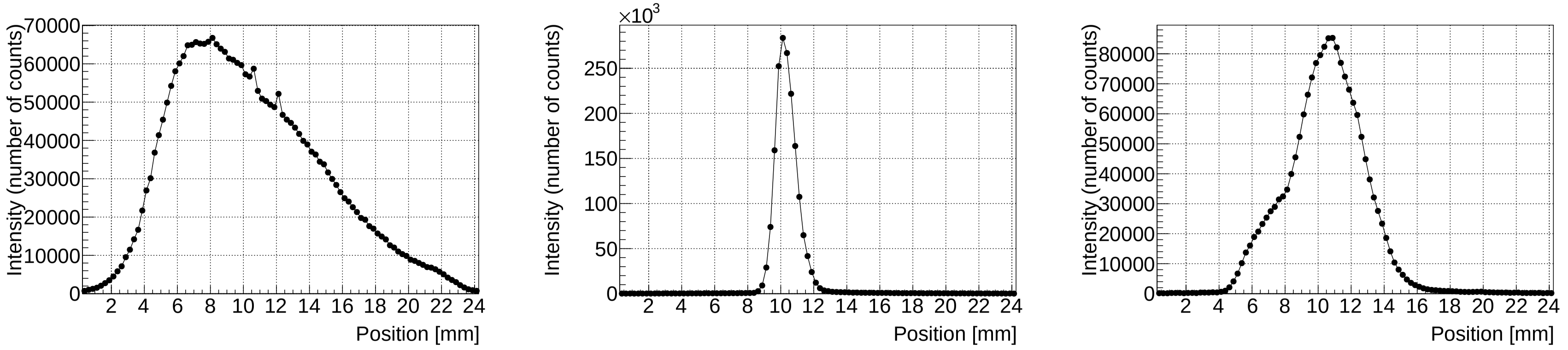

(a) Q_1 turned off.   **(b)** 20 A on Q_1.   **(c)** 30 A on Q_1.

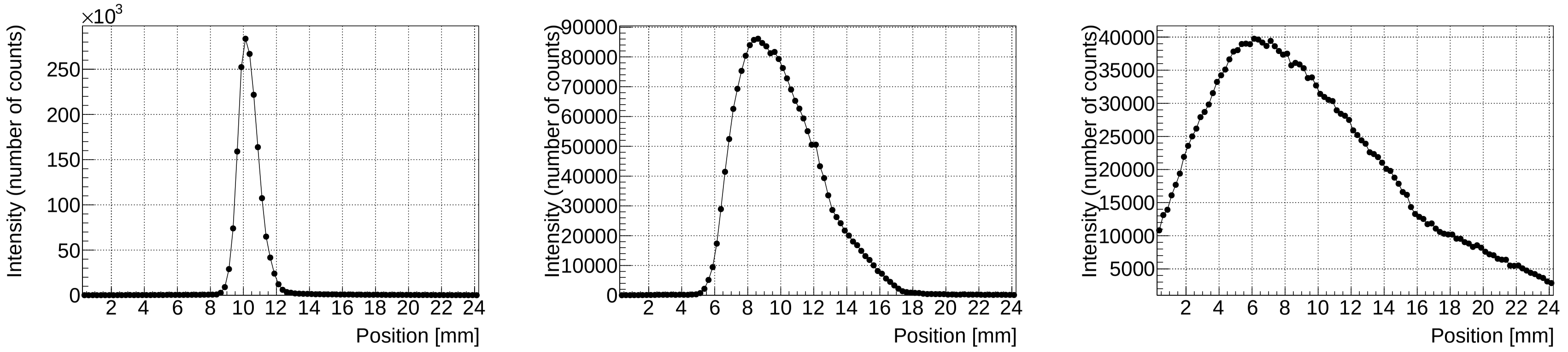

(d) Q_2 turned off.   **(e)** 20 A on Q_2.   **(f)** 50 A on Q_2.

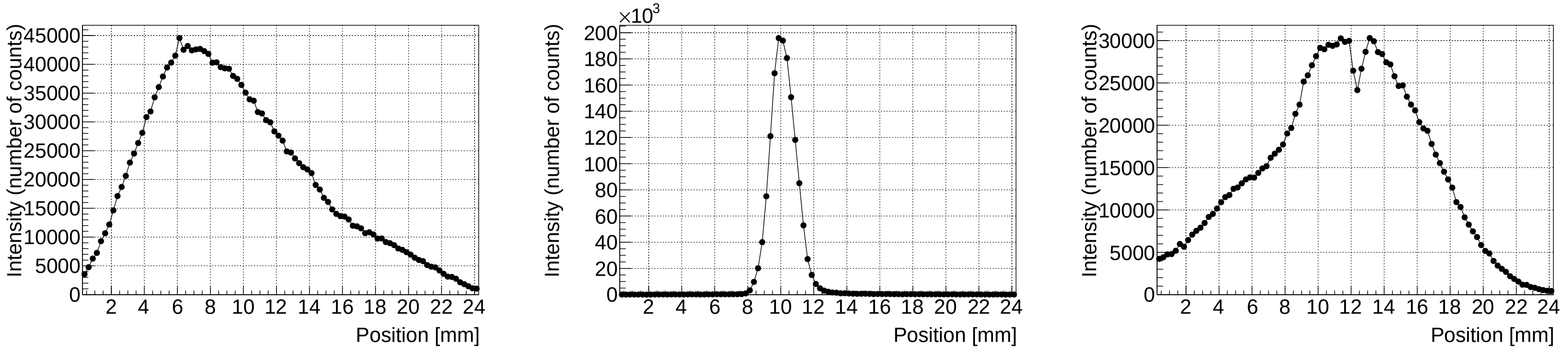

(g) 10 A on Q_1.   **(h)** 30 A on Q_1.   **(i)** 50 A on Q_1.

Figure 27: Horizontal beam profile development on UniBEaM 2.
Top: Q_2 turned off (blue).   Middle: 20 A on Q_1 (green).   Bottom: 20 A on Q_2 (red).

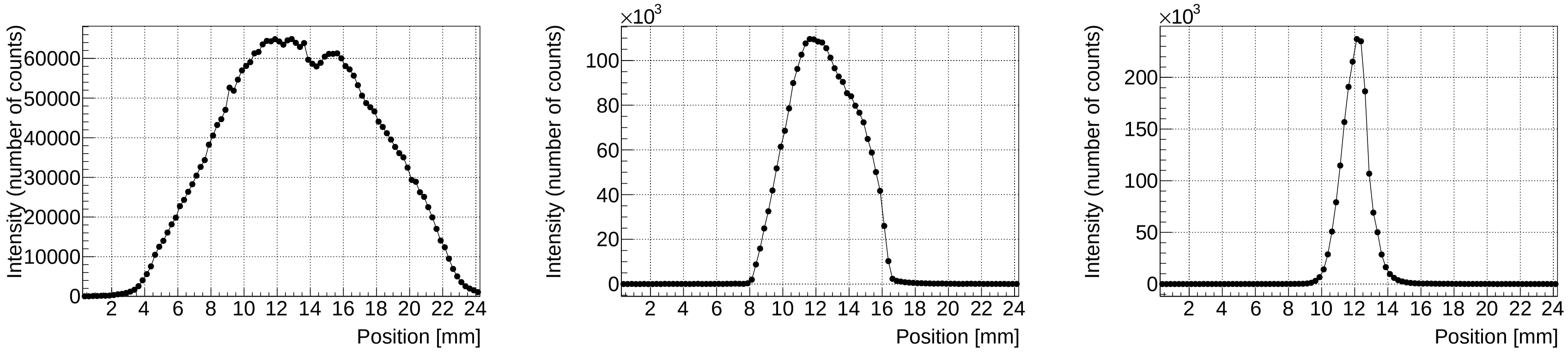

(a) Q_2 turned off.

(b) 40 A on Q_2.

(c) 75 A on Q_2.

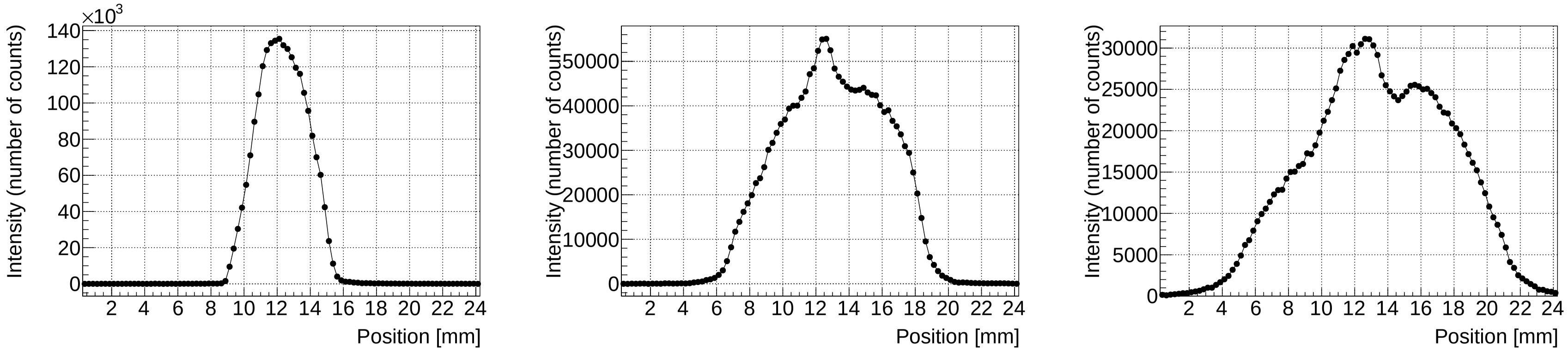

(d) Q_1 turned off.

(e) 40 A on Q_1.

(f) 75 A on Q_1.

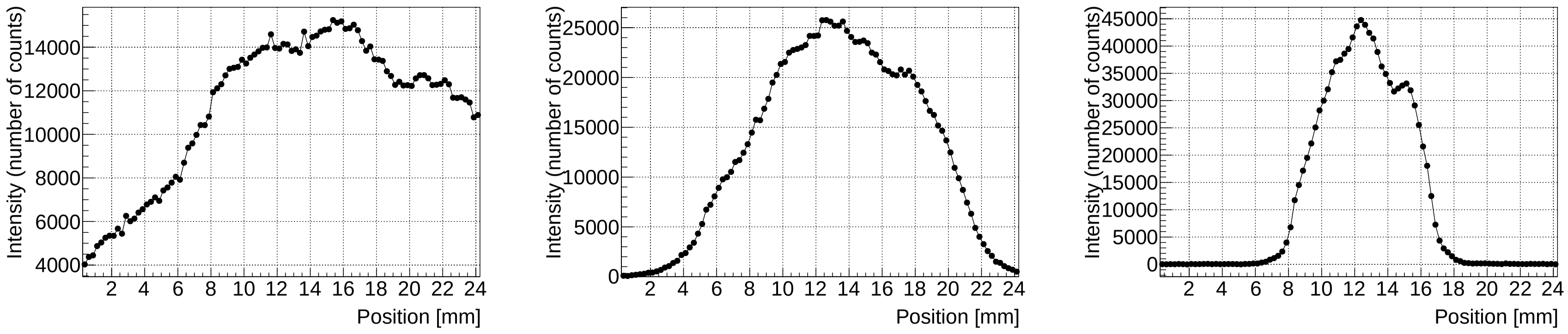

(g) Q_2 turned off.

(h) 40 A on Q_2.

(i) 75 A on Q_2.

Figure 28: Vertical beam profile development on UniBEaM 2.
Top: Q_1 turned off (blue). Middle: 50 A on Q_2 (green). Bottom: 50 A on Q_1 (red).

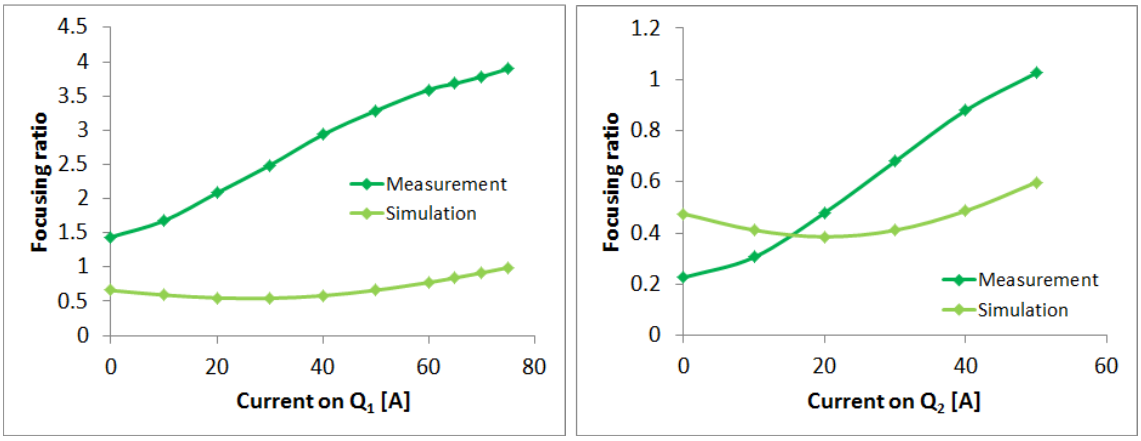

(a) Green curve of figure 19a
(50 A on Q_2, vertical profiles).

(b) Green curve of figure 19b
(20 A on Q_1, horizontal profiles).

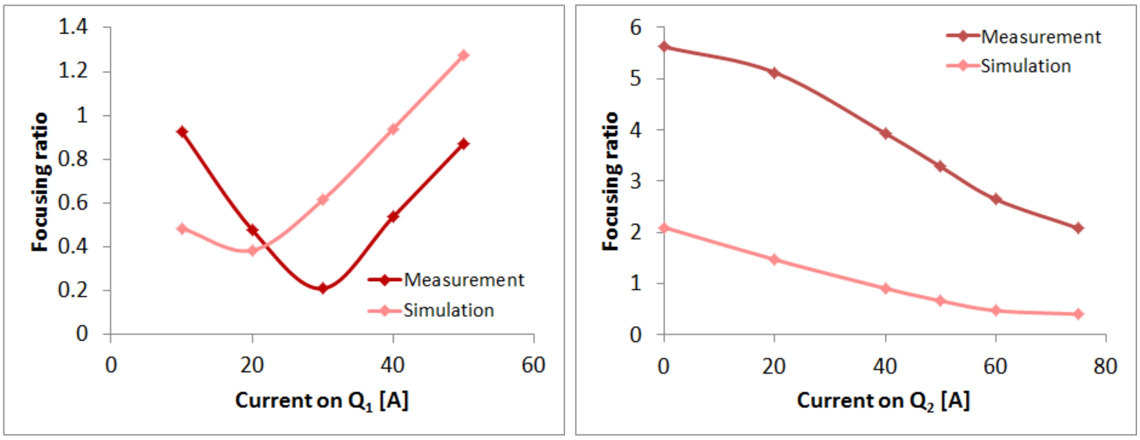

(c) Red curve of figure 19a
(20 A on Q_2, horizontal profiles).

(d) Red curve of figure 19b
(50 A on Q_1, vertical profiles).

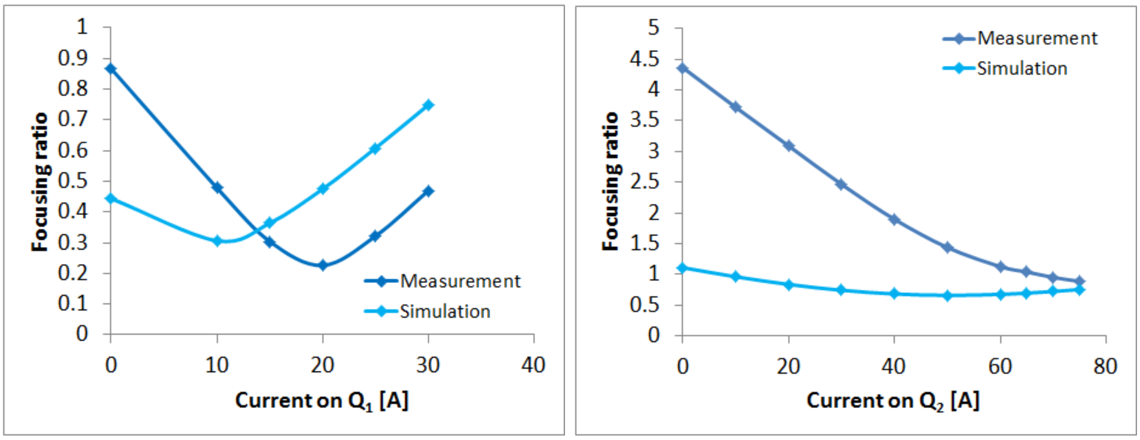

(e) Blue curve of figure 19a
(Q_2 turned off, horizontal profiles).

(f) Blue curve of figure 19b
(Q_1 turned off, vertical profiles).

Figure 29: Comparison of measurement and simulation.

Steering

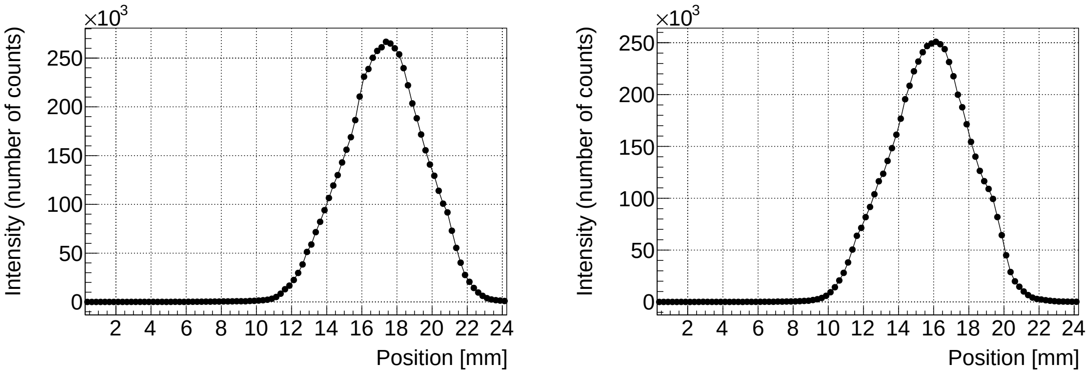

(a) Profile number 1 (I = 10 A).

(b) Profile number 2 (I = 5 A).

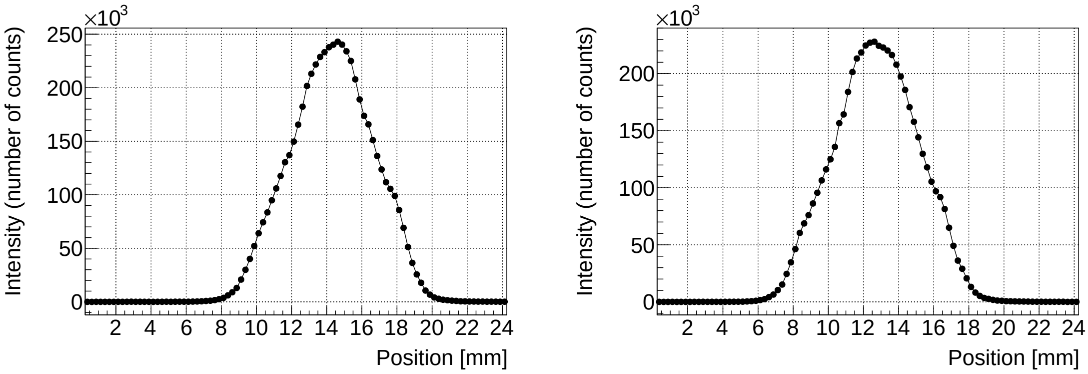

(c) Profile number 3 (I = 0 A).

(d) Profile number 4 (I = -5 A).

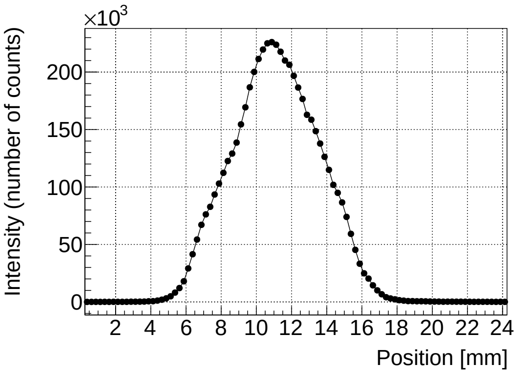

(e) Profile number 5 (I = -10 A).

Figure 30: Transversal profiles of the second UniBEaM detector for the vertical steering measurement. The profile numbers refer to the ones in table 6.